Electronic Supplementary Information (ESI)

Crystal structure – solid-state CPMAS ^{13}C NMR correlation in luminescent d^{10} metal-organic frameworks constructed with the 1,2-bis(1,2,4-triazol-4-yl)ethane ligand

Hesham A. Habib,[a] Anke Hoffmann,*[,b] Henning A. Höppe,[a] Gunther Steinfeld [a] and Christoph Janiak*[,a]

[a] *Institut für Anorganische und Analytische Chemie, Universität Freiburg, Albertstr. 21, D-79104 Freiburg, Germany. E-mail: janiak@uni-freiburg.de; Fax: 49 761 2036147; Tel: 49 761 2036127*
[b] *Institut für Makromolekulare Chemie, Universität Freiburg, Stefan-Meier-Str. 31, D-79104 Freiburg, Germany. E-mail: anke.hoffmann@makro.uni-freiburg.de; Fax: +49 761 2036306; Tel: +49 761 203631*

Content

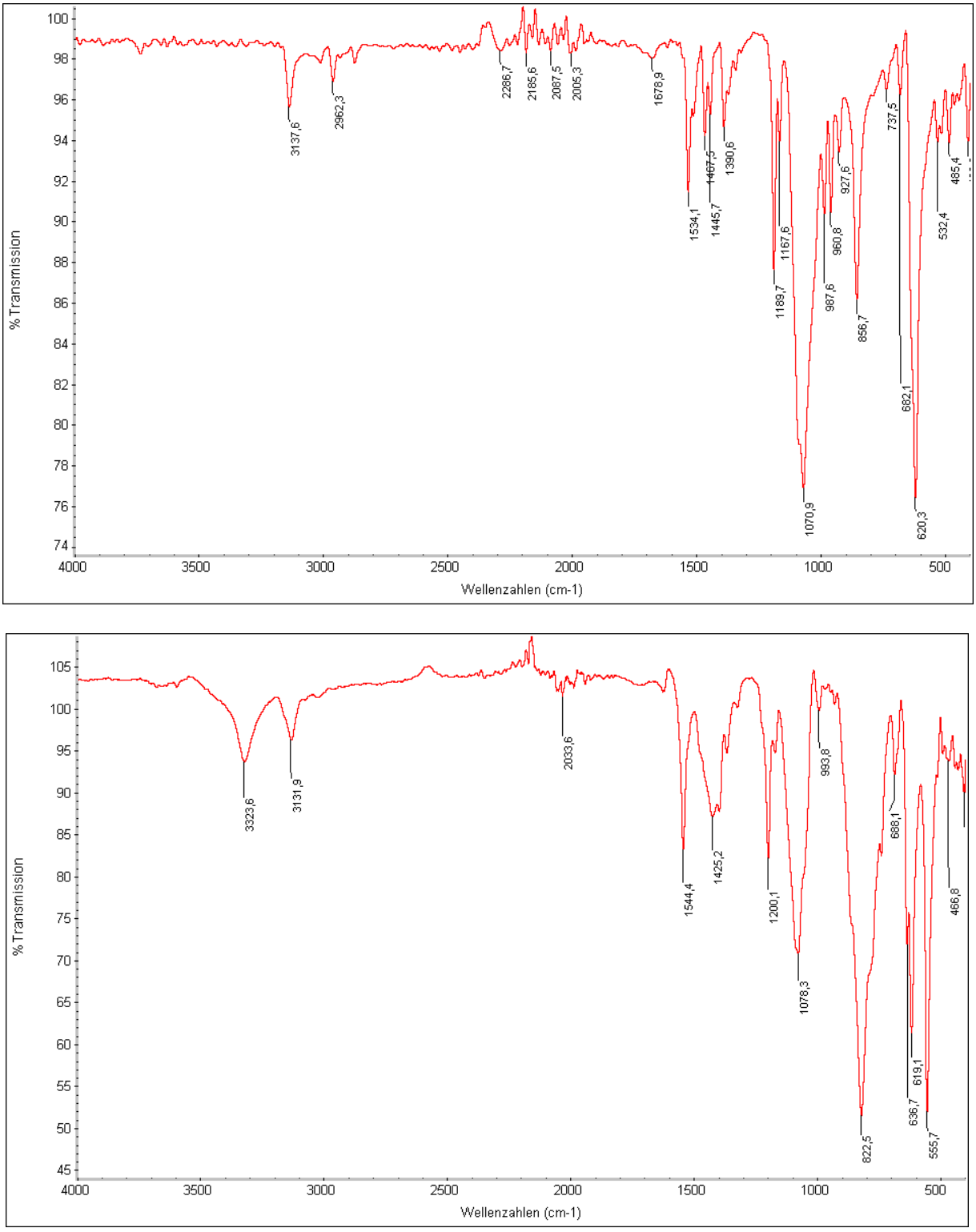

Fig. S1 Infrared spectrum of the ClO_4^--containing 3D-framework **7** (top) and the PF_6^--containing framework **7'** (bottom) from a 24 h reaction of crystals of **7** in 3 mol/l aqueous NH_4PF_6 solution.

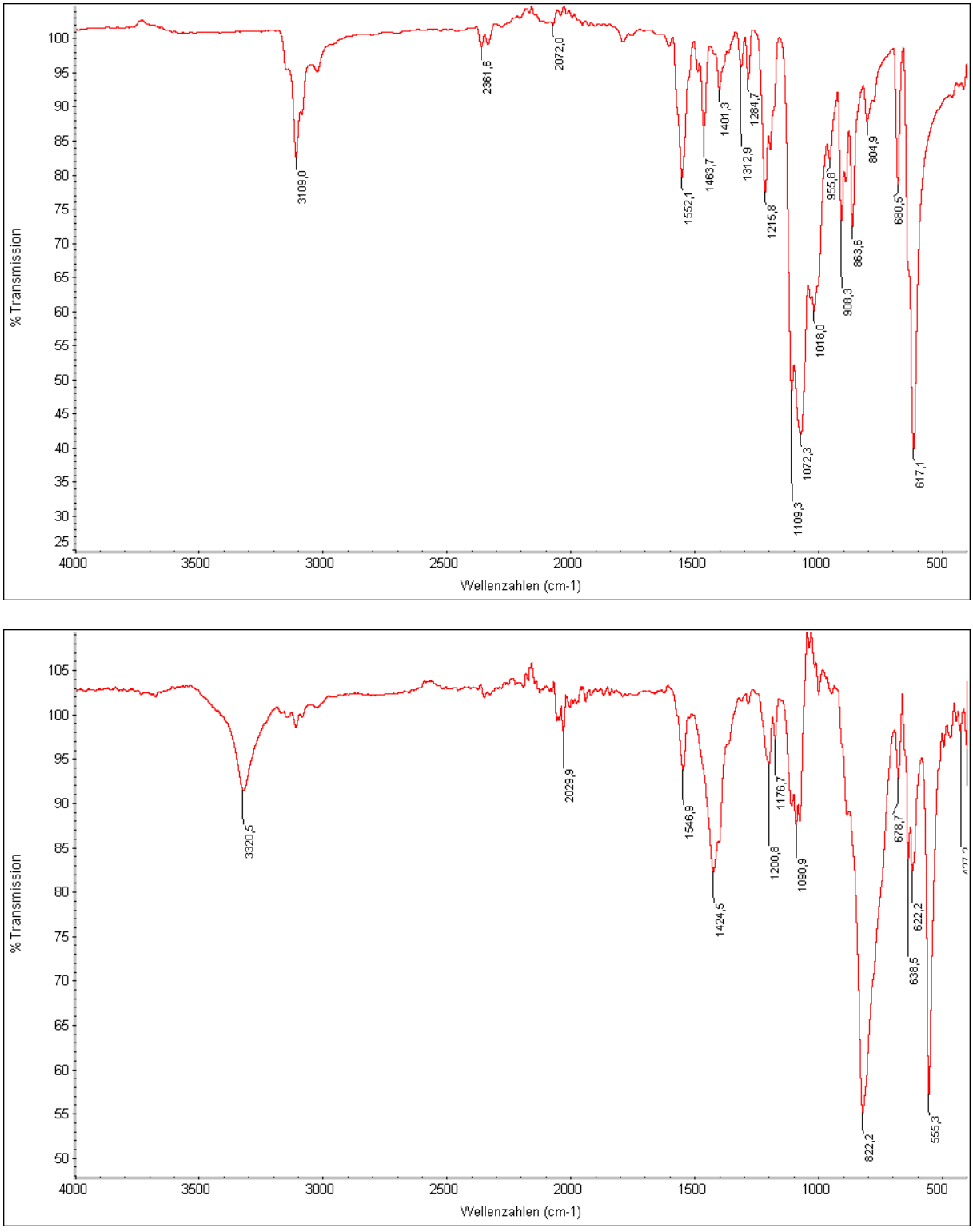

Fig. S2 Infrared spectrum of the ClO_4^--containing 3D-framework **8** (top) and the PF_6^--containing material **8'** (bottom) from a 24 h reaction of crystals of **8** in 3 mol/l aqueous NH_4PF_6 solution.

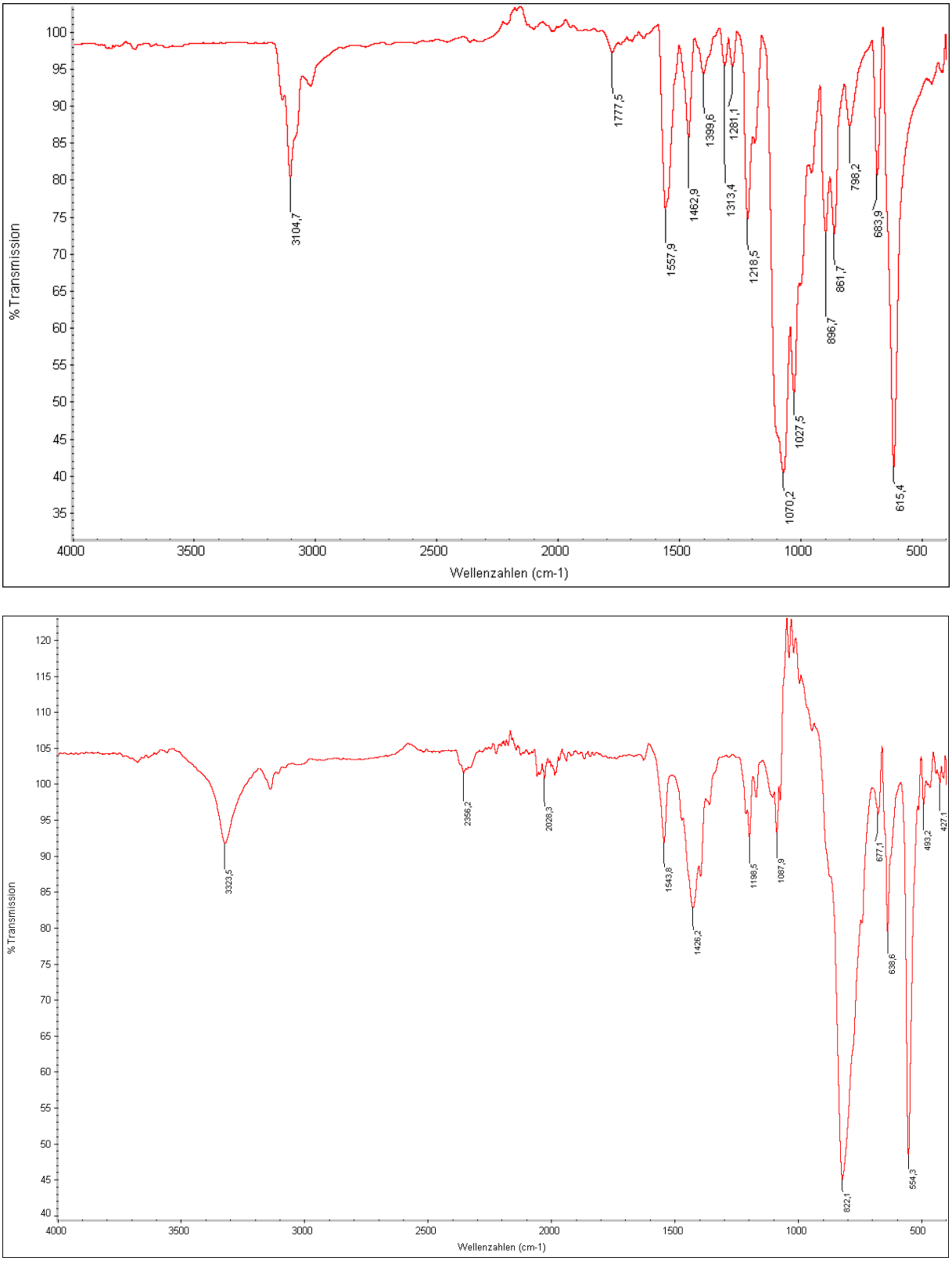

Fig. S3 Infrared spectrum of the ClO_4^--containing 3D-framework **9** (top) and the PF_6^--containing framework **9'** (bottom) from a 24 h reaction of crystals of **9** in 3 mol/l aqueous NH_4PF_6.

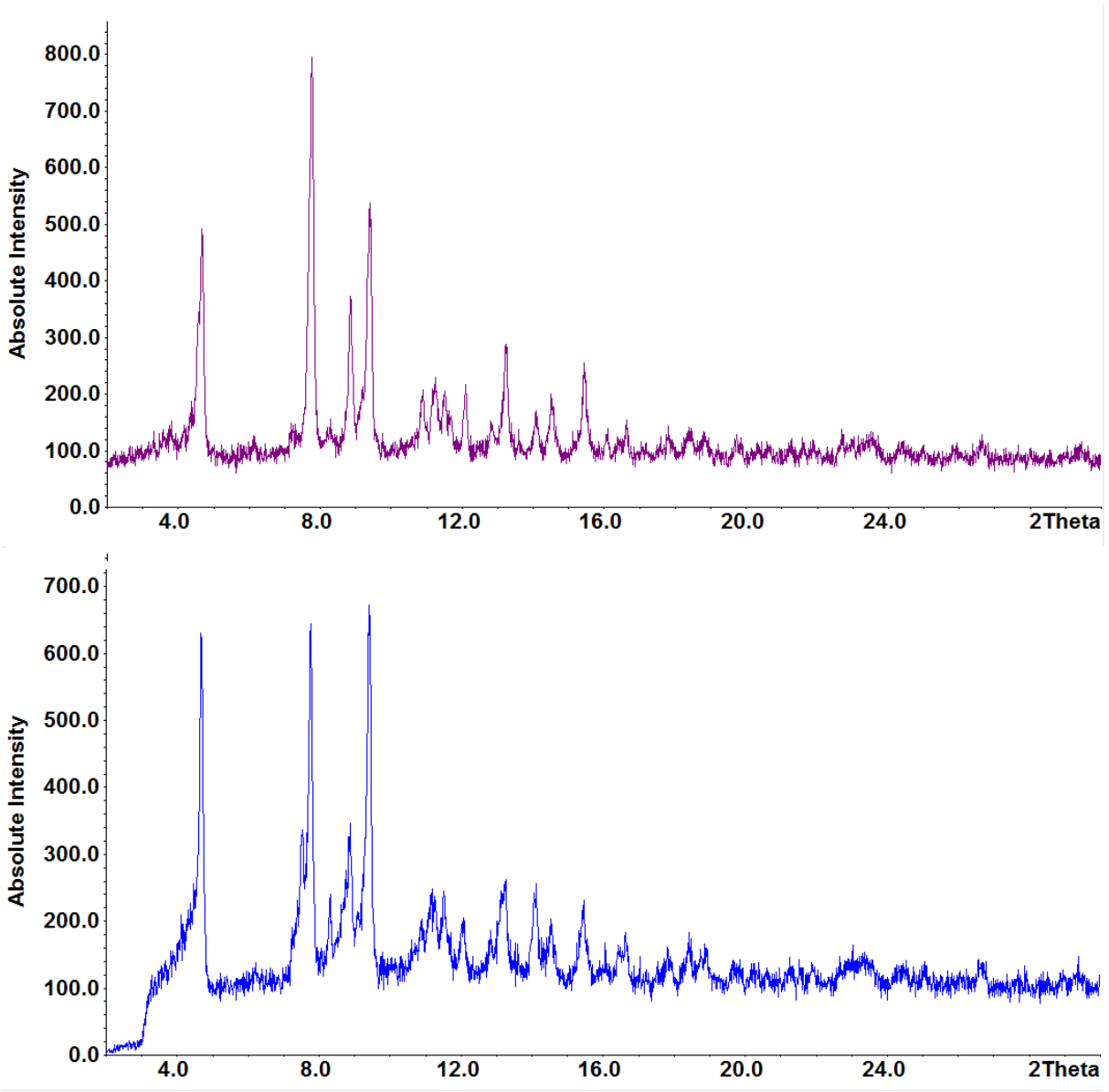

Fig. S4 X-ray powder diffractogram of the ClO_4^--containing 3D-framework **7** (top) and the PF_6^--containing framework **7'**(bottom) from a 24 h reaction of crystals of **7** in 3 mol/l aqueous NH_4PF_6 solution.

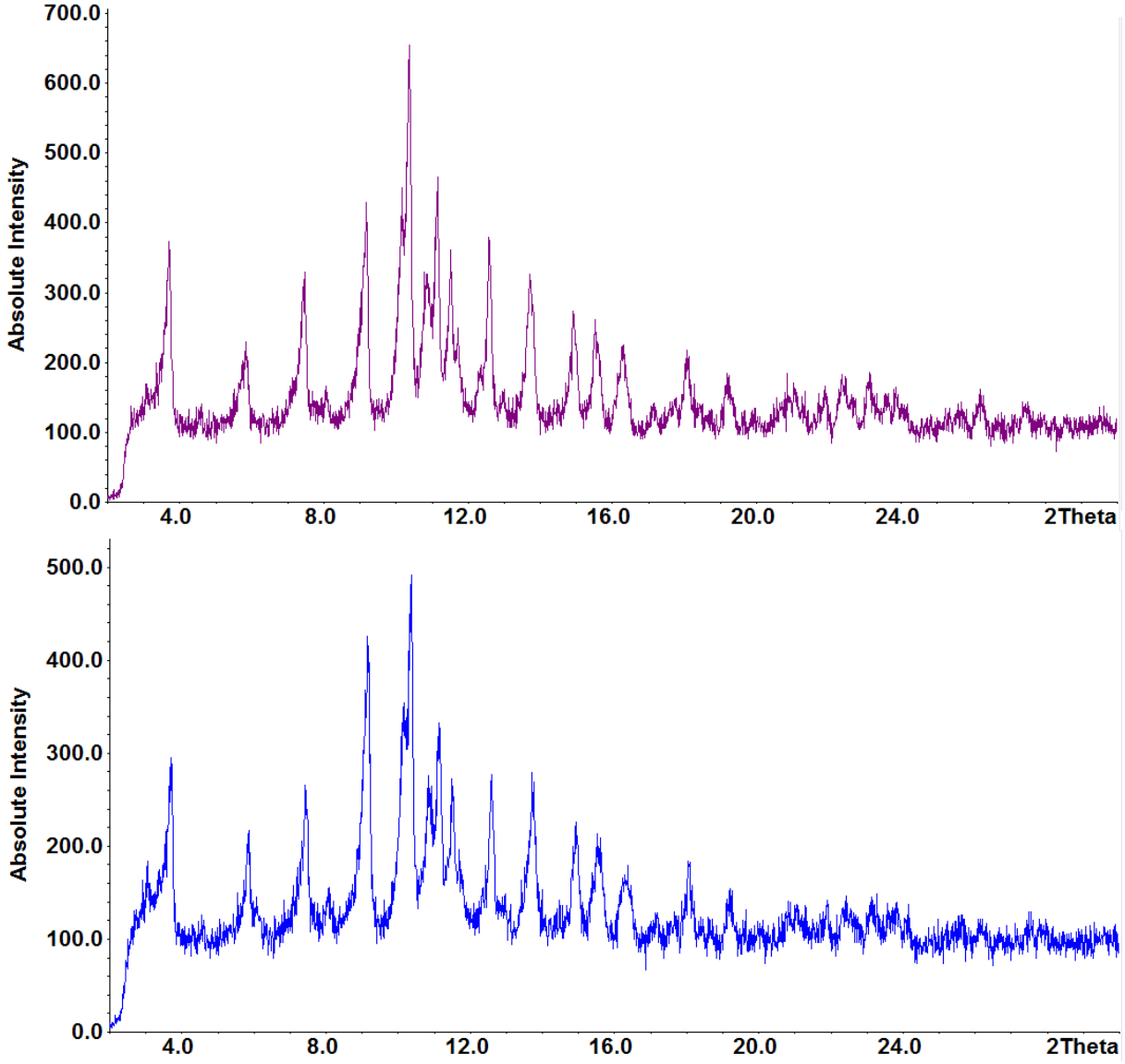

Fig. S5 X-ray powder diffractogram of the ClO_4^--containing 3D-framework **8** (top) and the PF_6^--containing framework **8'**(bottom) from a 24 h reaction of crystals of **8** in 3 mol/l aqueous NH_4PF_6 solution.

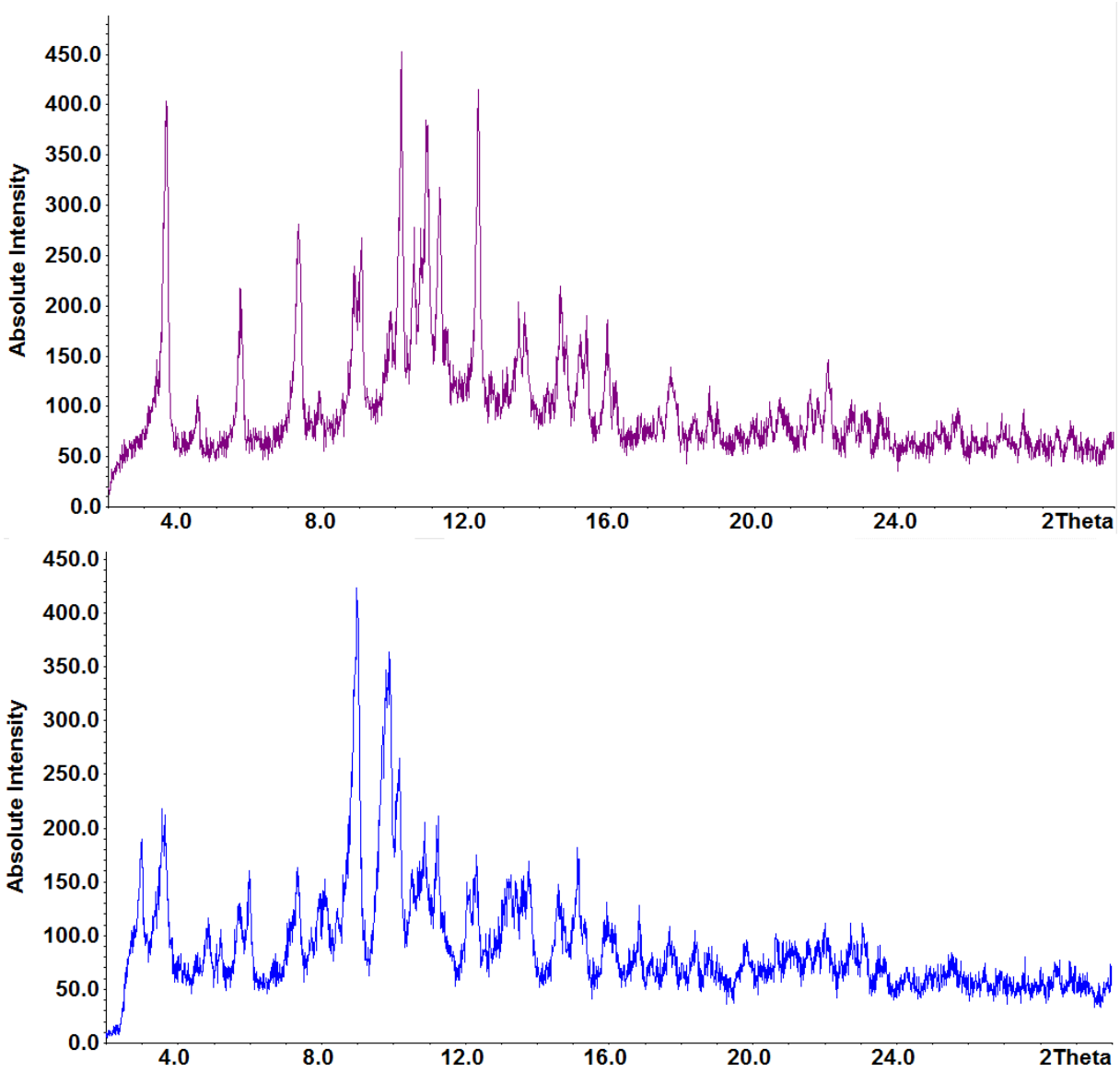

Fig. S6 X-ray powder diffractogram of the ClO_4^--containing 3D-framework **9** (top) and the PF_6^--containing framework **9'**(bottom) from a 24 h reaction of crystals of **9** in 3 mol/l aqueous NH_4PF_6 solution.

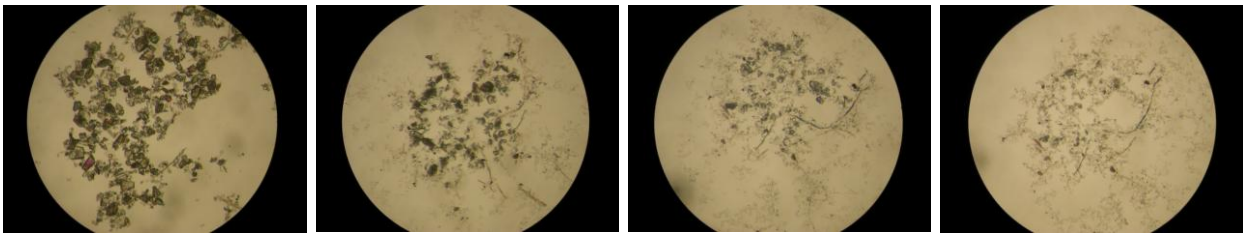

Fig. S7 Photographs of (a) crystals of the ClO_4^--containing 3D-framework **8** directly after immersion in aqueous NH_4PF_6 solution at t = 0 h, (b) the same section of the reaction dish after 6 h, (c) after 12 h and (d) after 24 h at which time the material analyzed as a PF_6^--containing framework **8'** (cf. Fig. S2 and S5)

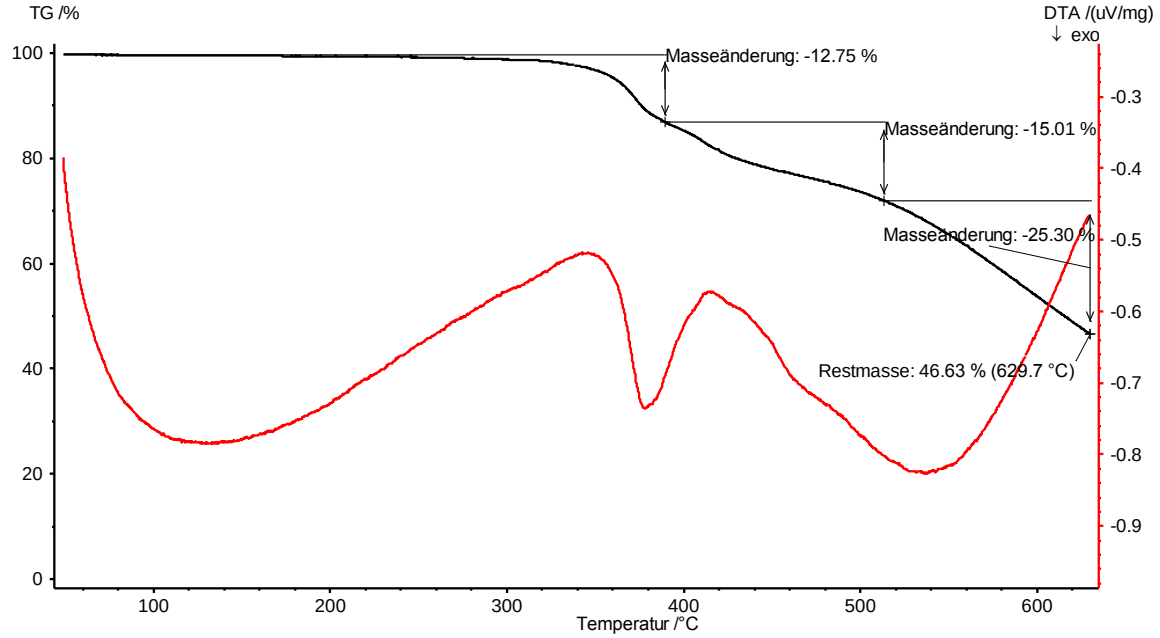

Fig. S8 Thermogravimetric analysis of [{$ZnCl_2(\mu_2$-btre)}$_2$] (**1**) under nitrogen after a vacuum cycle (STA 409 from Netzsch, heating rate: 10 K min^{-1}, N_2 flow rate: 75 ml/min).
The weight loss in the temperature range 300-390 corresponds to the removal of half of the btre ligands (obs. 12.8, calcd. 13.7%). The immediately following second weight loss in the range 390-515 °C includes the removal of the second half of btre molecules (obs. 15.0, calcd. 13.7%). The continuing weight loss until over 600 °C matches with the loss of the second btre ligand (obs. 25.3, calcd. 27.3%) with a remaining 46.6% for $ZnCl_2$ (calcd. 45.4%).

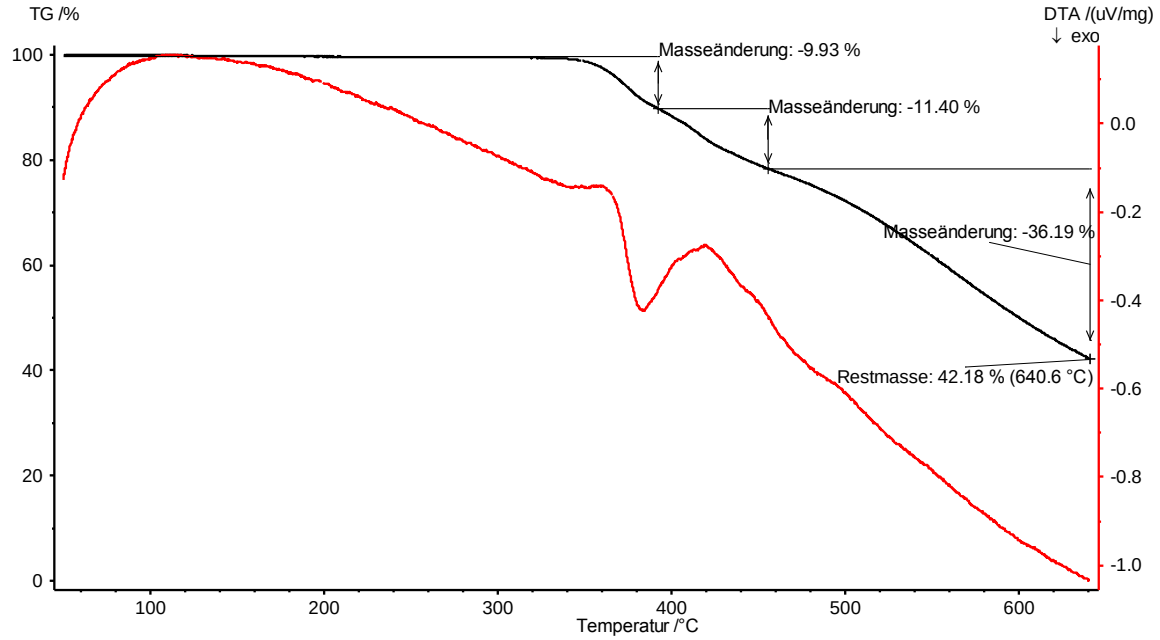

Fig. S9 Thermogravimetric analysis of [{$ZnBr_2(\mu_2$-btre)}$_2$] (**2**) under nitrogen after a vacuum cycle (STA 409 from Netzsch, heating rate: 10 K min^{-1}, N_2 flow rate: 75 ml/min).
The weight loss in the temperature range 330-390 °C corresponds to the removal of half of the btre ligands (obs. 9.9, calcd. 10.5%). The immediately following second weight loss in the 390-455 °C includes the removal of the second half of btre molecules (obs. 11.4, calcd. 10.5%). The continuing weight loss until over 600 °C includes the loss of the second btre ligand (calcd. 21.1%).

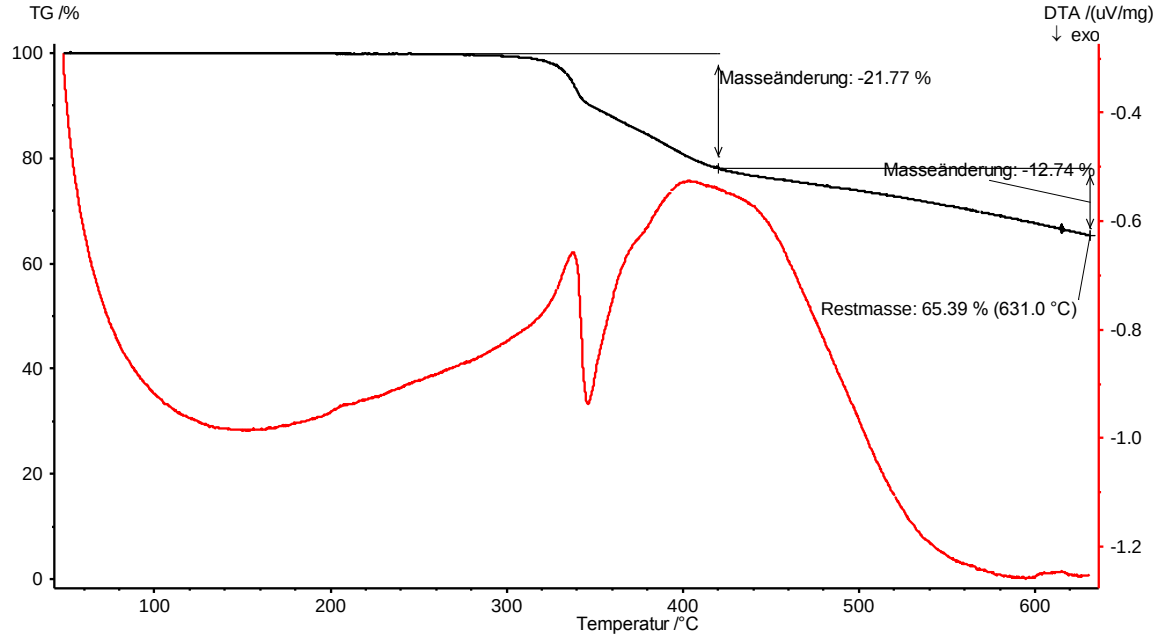

Fig. S10 Thermogravimetric analysis of $^{2}_{\infty}[Cu_2(\mu_2\text{-}Cl)_2(\mu_4\text{-btre})]$ (**4**) under nitrogen after a vacuum cycle (simultaneous thermoanalysis apparatus STA 409 from Netzsch, heating rate: 10 K min^{-1}, N_2 flow rate: 75 ml/min).
The weight loss in the temperature range 270-420 °C corresponds to the removal of half of the btre ligand (obs. 21.8, calcd. 22.7%).

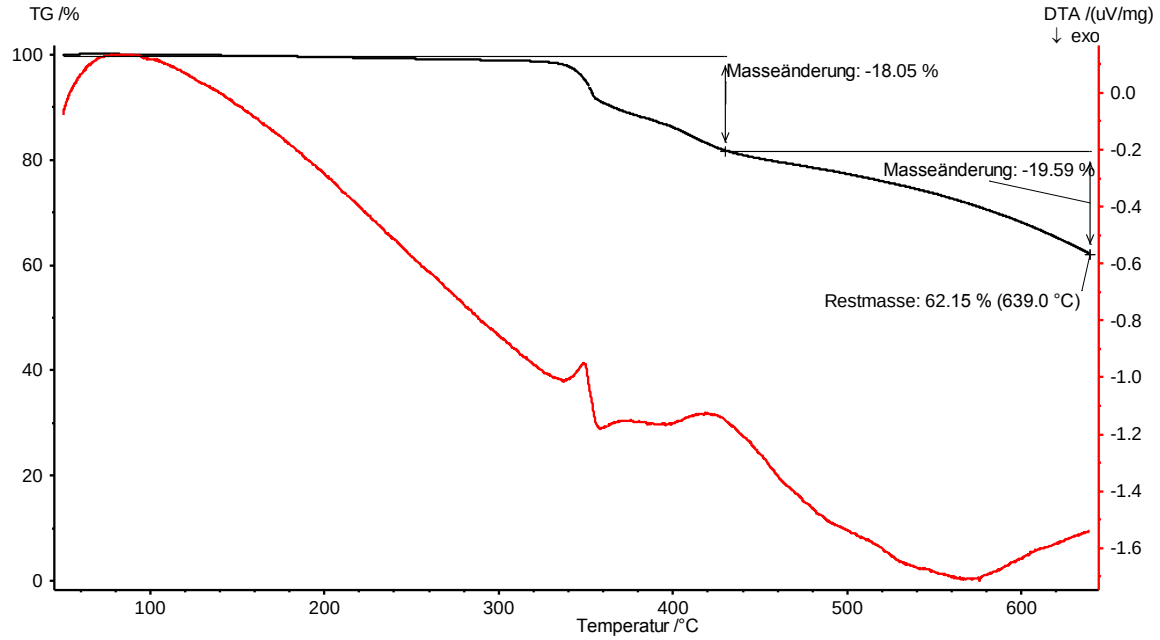

Fig. S11 Thermogravimetric analysis of $^{2}_{\infty}[Cu_2(\mu_2\text{-}Br)_2(\mu_4\text{-btre})]$ (**5**) under nitrogen after a vacuum cycle (simultaneous thermoanalysis apparatus STA 409 from Netzsch, heating rate: 10 K min^{-1}, N_2 flow rate: 75 ml/min).
The weight loss in the temperature range 330-430 °C corresponds to the removal of half of the btre ligand (obs. 18.1, calcd. 18.2%). The loss of the full btre ligand calculates as 36.4%.

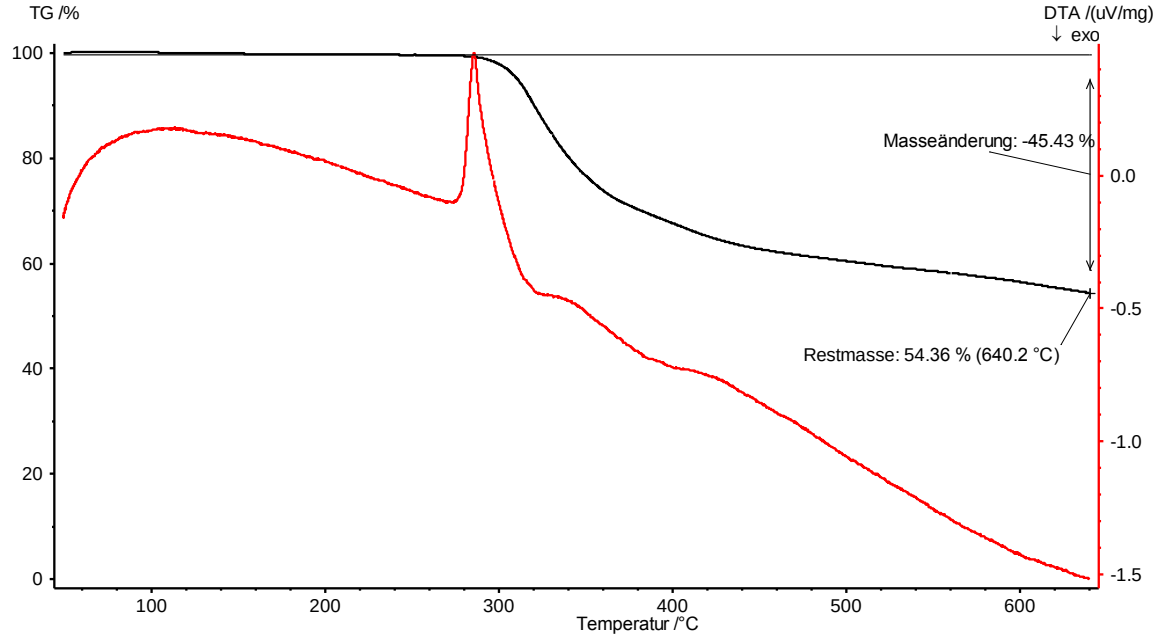

Fig. S12 Thermogravimetric analysis of $^{1}_{\infty}$[Zn(NCS)$_2$(μ$_2$-btre)] (**3**) under nitrogen after a vacuum cycle. Thermogravimetric analyses were carried out on a simultaneous thermoanalysis apparatus STA 409 from Netzsch under nitrogen (heating rate: 10 K min^{-1}, N_2 flow rate: 75 ml/min).

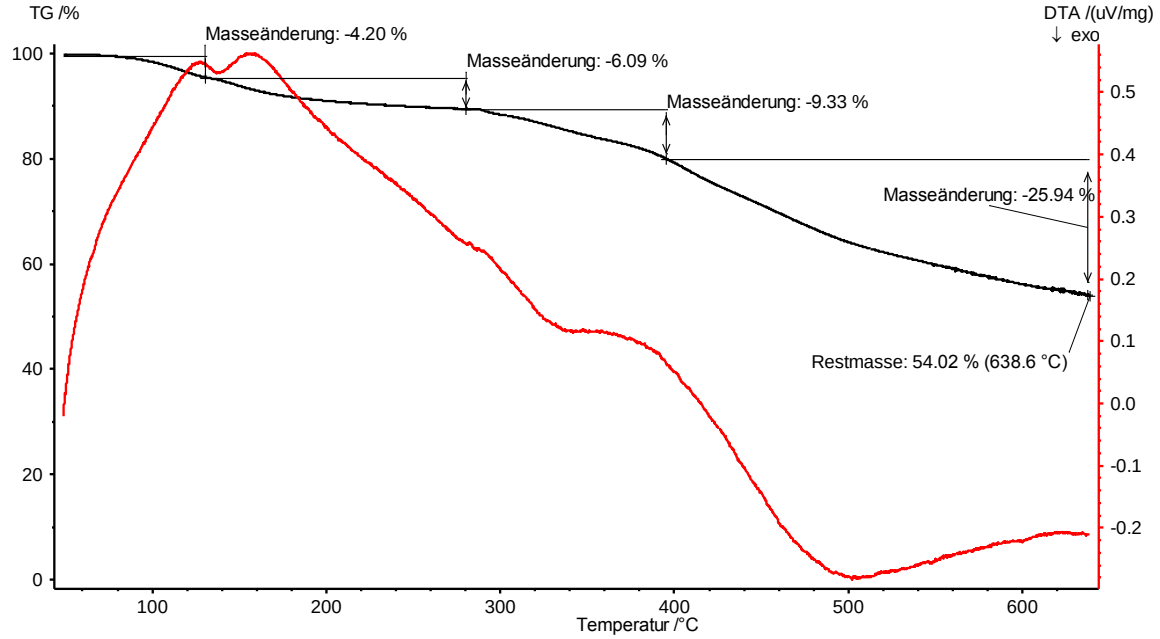

Fig. S13 Thermogravimetric analysis of $^{2}_{\infty}${[Cd$_6$(μ$_3$-OH)$_2$(μ$_3$-SO$_4$)$_4$(μ$_4$-btre)$_3$(H$_2$O)$_6$](SO$_4$) · ~6H$_2$O} (**6**) under nitrogen after a vacuum cycle (simultaneous thermoanalysis apparatus STA 409 from Netzsch, heating rate: 10 K min^{-1}, N_2 flow rate: 75 ml/min).
A weight loss in the range 290-395 °C of around 9.3% is assigned to the removal of one btre ligand in the above sum formula (calcd. 8.7%). The overall weight loss from 290 to over 600 °C of 35.3% includes the loss of all btre ligands (calcd. 26.0%).

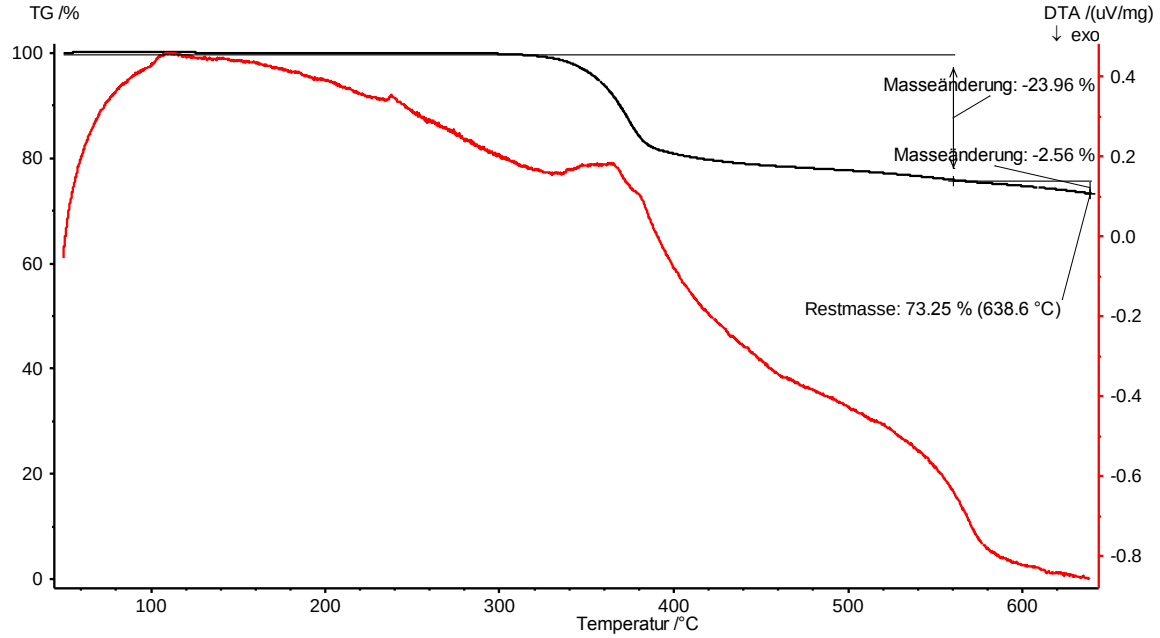

Fig. S14 Thermogravimetric analysis of $^{3}_{\infty}[Cu_2(\mu_2\text{-}CN)_2(\mu_4\text{-btre})]$ (**10**) under nitrogen after a vacuum cycle (simultaneous thermoanalysis apparatus STA 409 from Netzsch, heating rate: 10 K min^{-1}, N_2 flow rate: 75 ml/min).

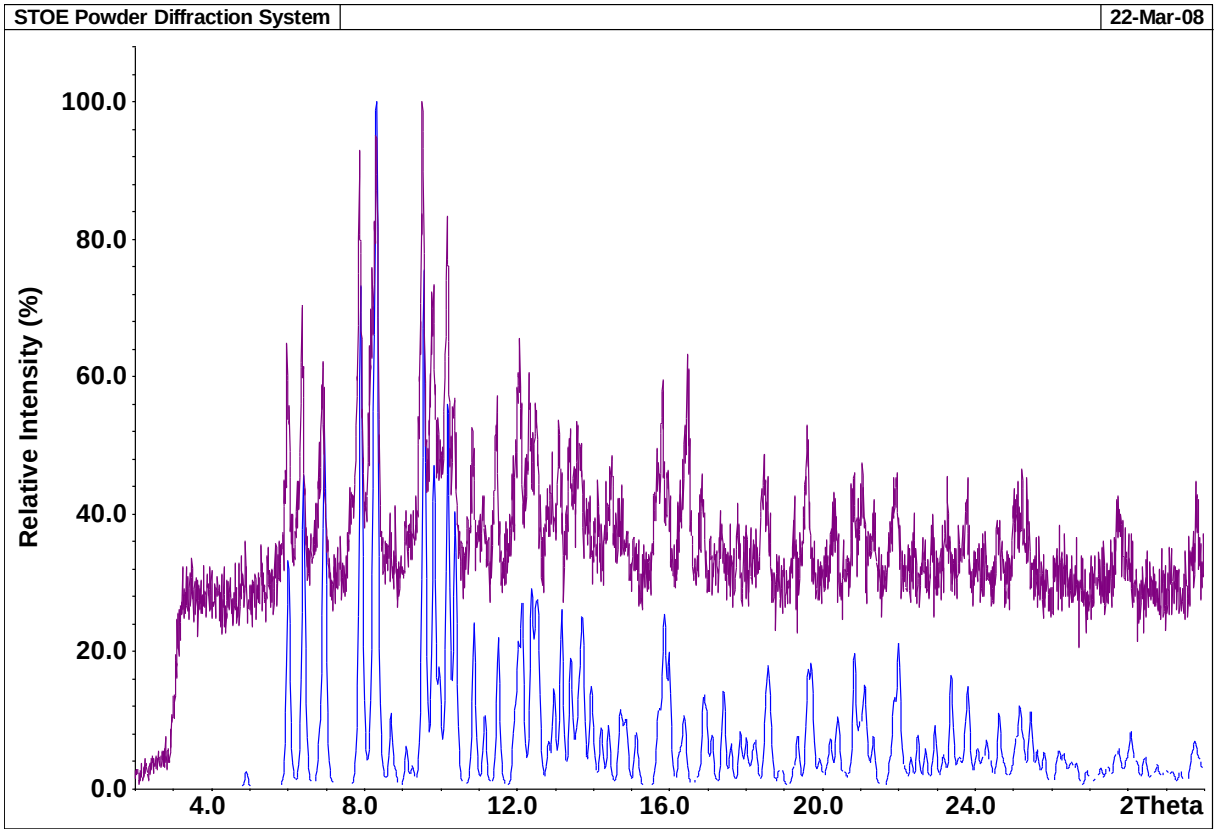

Fig. S15 X-ray powder diffractogram. Blue curve is simulated from single-crystal X-ray data of $[\{ZnCl_2(\mu_2\text{-btre})\}_2]$ (**1**). Purple curve is measured on a crystal sample of **1**.

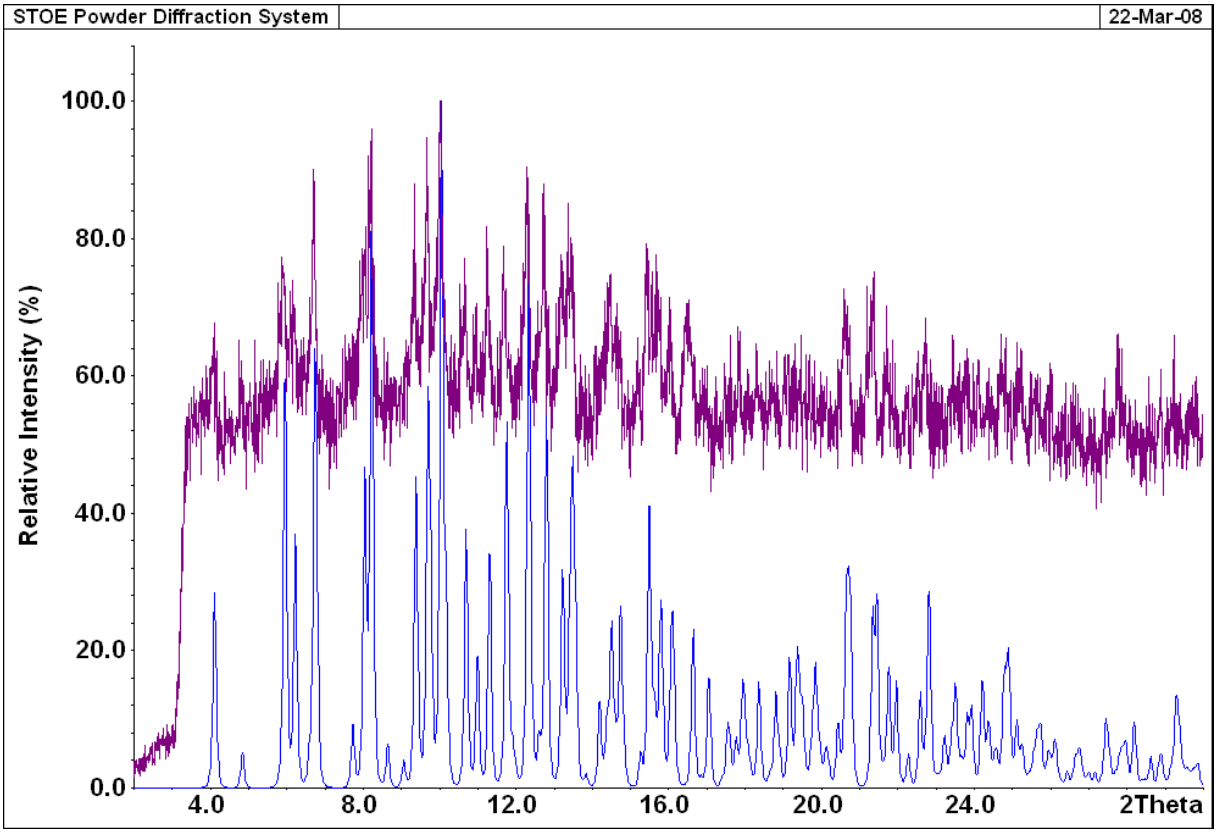

Fig. S16 X-ray powder diffractogram. Blue curve is simulated from single-crystal X-ray data of [{$ZnBr_2(\mu_2$-btre)}$_2$] (**2**). Purple curve is measured on a crystal sample of **2**.

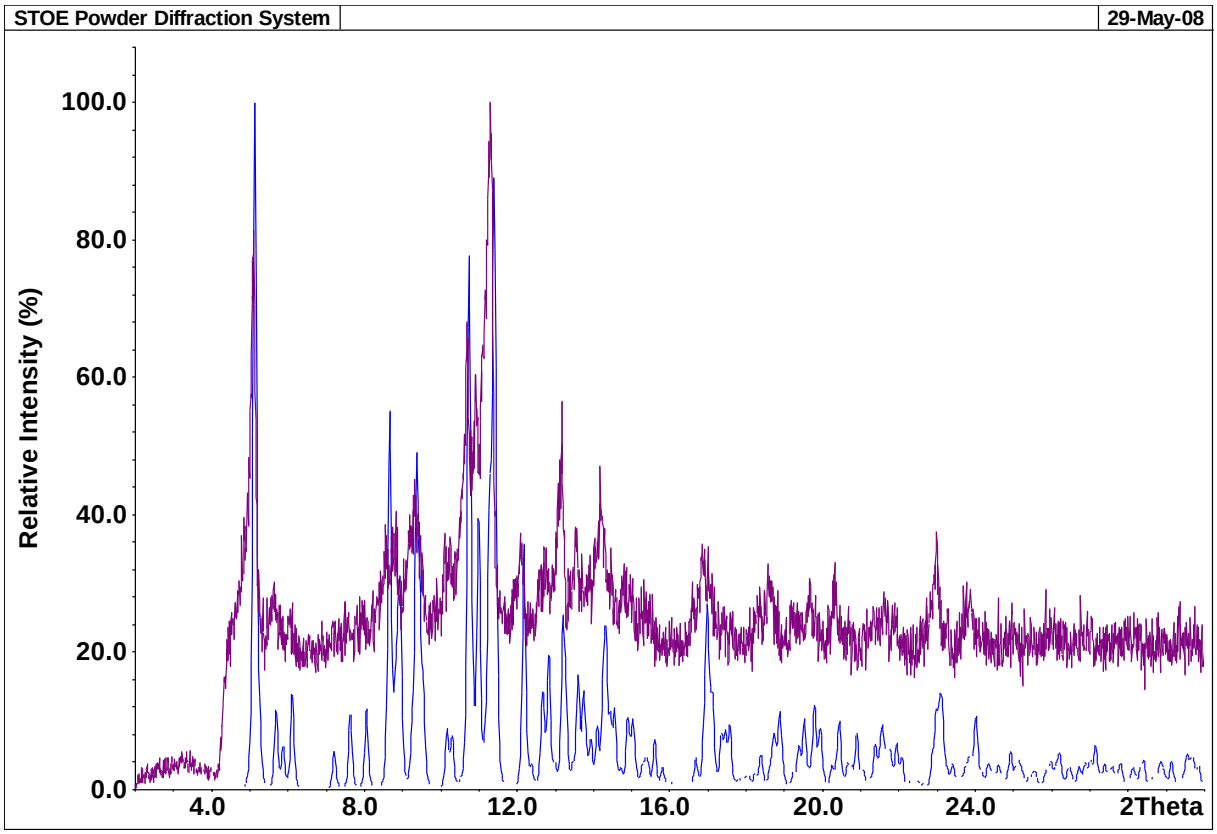

Fig. S17 X-ray powder diffractogram. Blue curve is simulated from single-crystal X-ray data of $^1{}_\infty$[$Zn(NCS)_2(\mu_2$-btre)] (**3**). Purple curve is measured on a crystal sample of **3**.

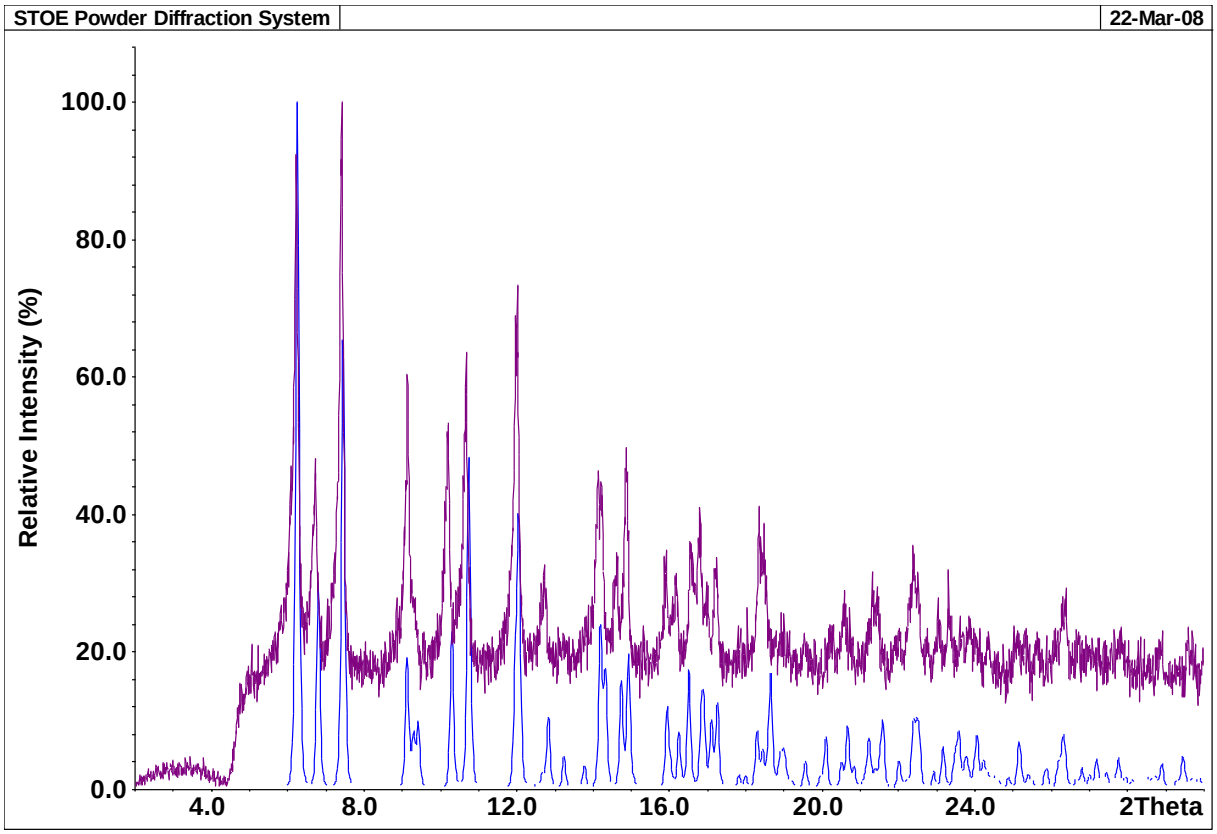

Fig. S18 X-ray powder diffractogram. Blue curve is simulated from single-crystal X-ray data of $^{2}_{\infty}[Cu_2(\mu_2\text{-}Cl)_2(\mu_4\text{-}btre)]$ (**4**). Purple curve is measured on a crystal sample of **4**.

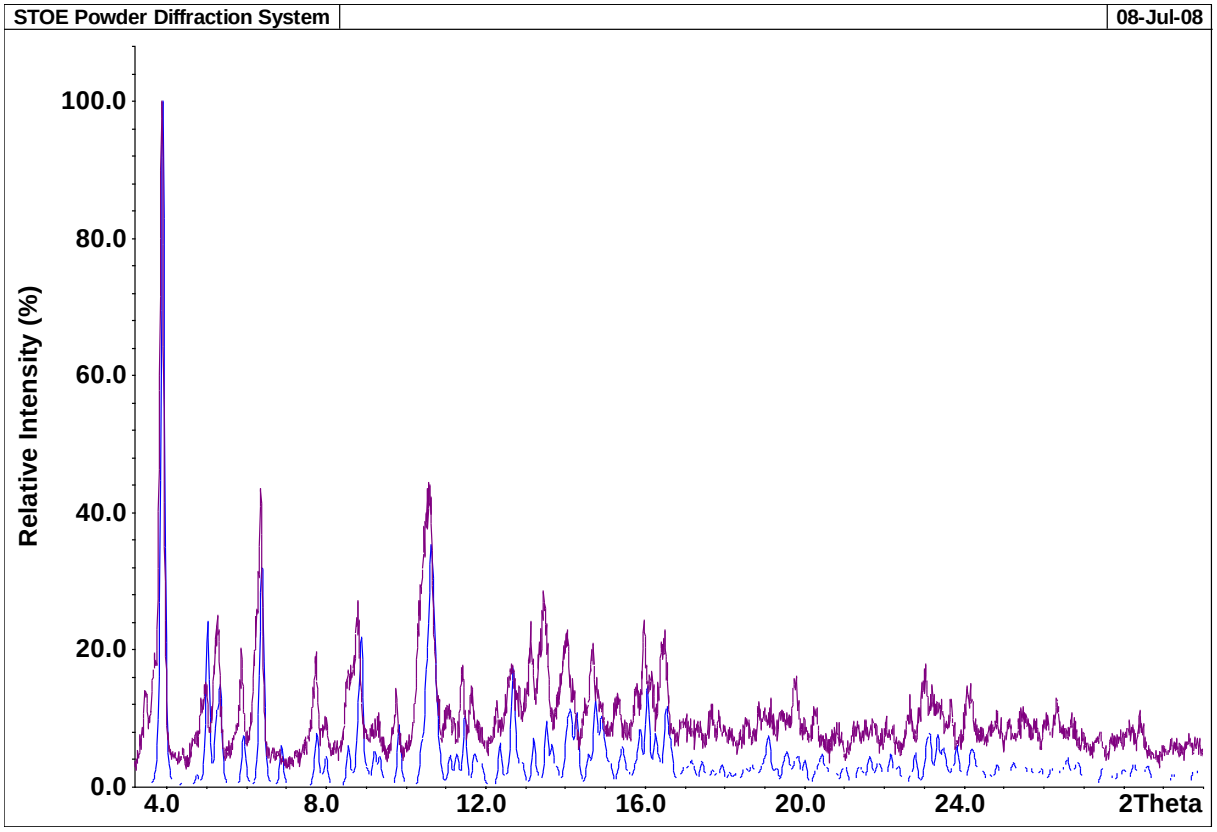

Fig. S19 X-ray powder diffractogram. Blue curve is simulated from single-crystal X-ray data of $^{2}_{\infty}\{[Cd_6(\mu_3\text{-}OH)_2(\mu_3\text{-}SO_4)_4(\mu_4\text{-}btre)_3(H_2O)_6](SO_4) \cdot \sim 6H_2O\}$ (**6**). Purple curve is measured on a crystal sample of **6**.

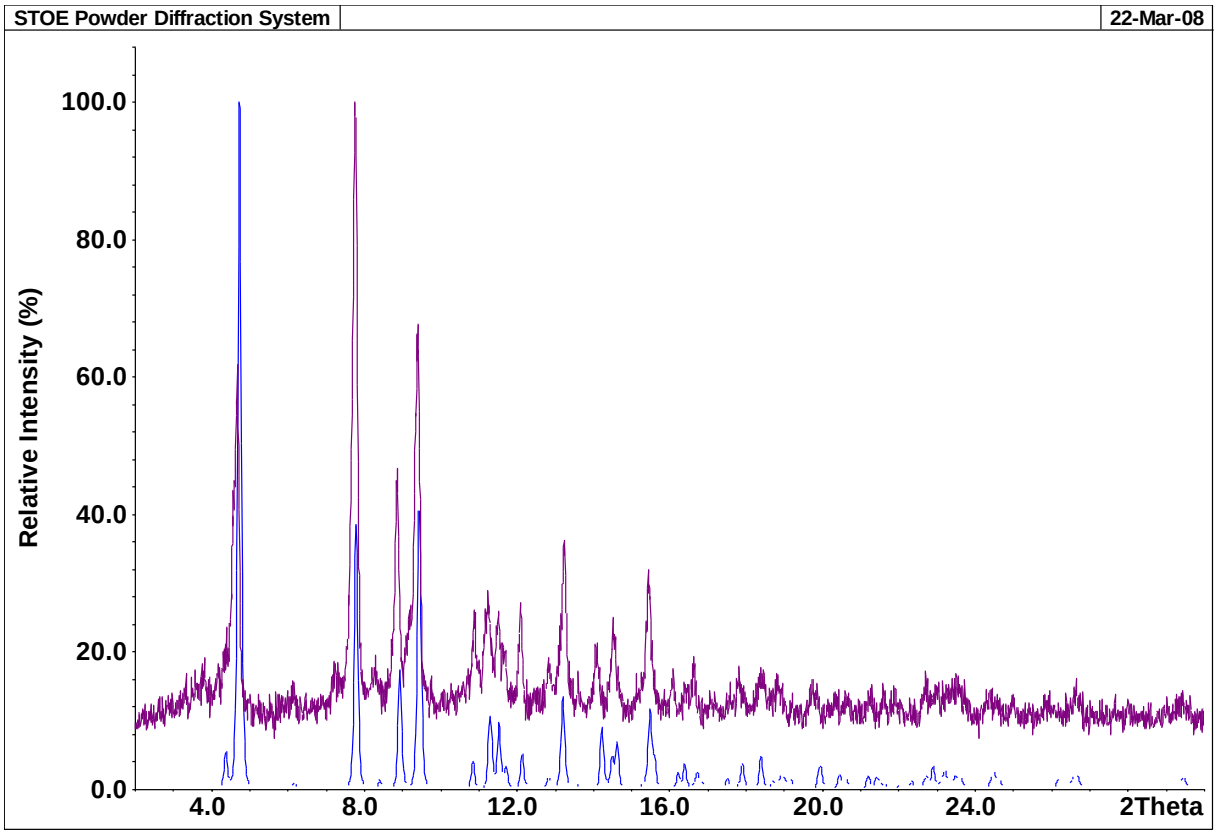

Fig. S20 X-ray powder diffractogram. Blue curve is simulated from single-crystal X-ray data of $^{3}_{\infty}${[Cu(μ_4-btre)]ClO_4 · ~0.25H_2O} (**7**). Purple curve is measured on a crystal sample of **7**.

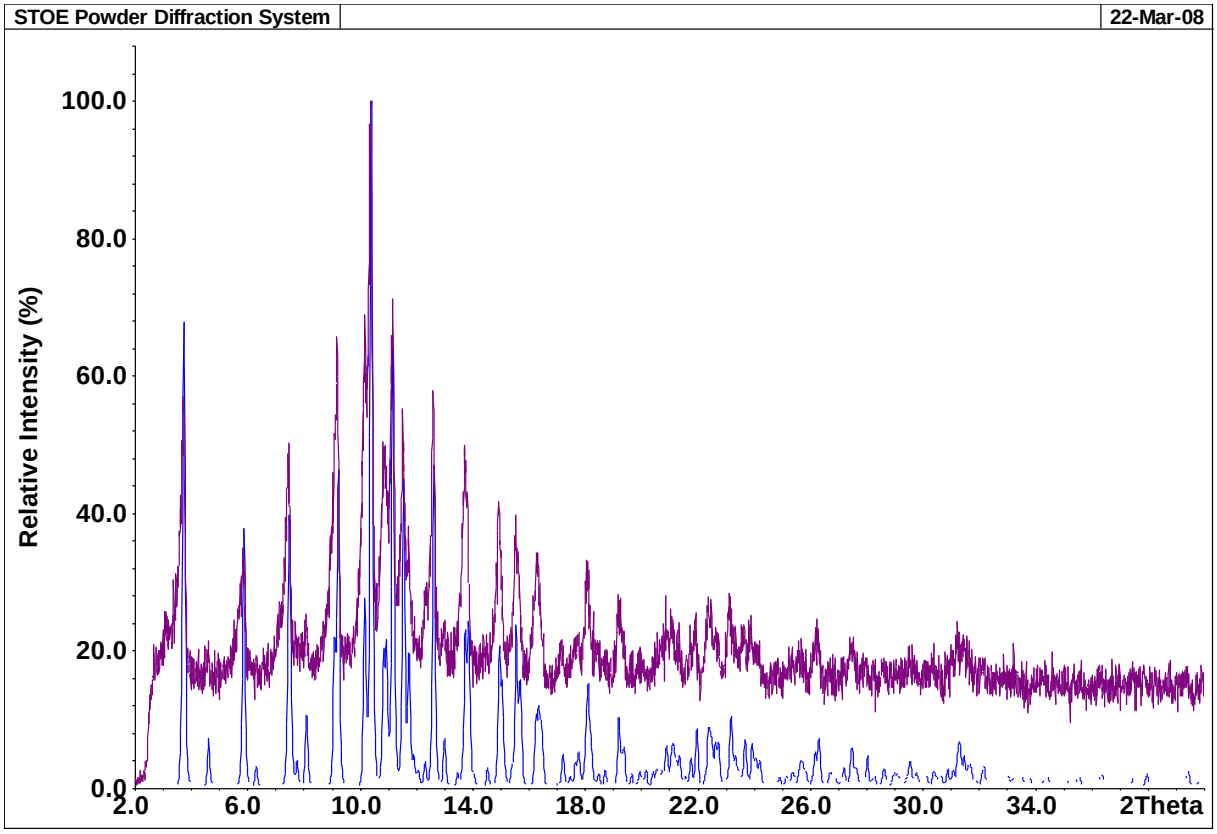

Fig. S21 X-ray powder diffractogram. Blue curve is simulated from single-crystal X-ray data of $^{3}_{\infty}${[Zn(μ_4-btre)(μ_2-btre)]$(ClO_4)_2$} (**8**). Purple curve is measured on a crystal sample of **8**.

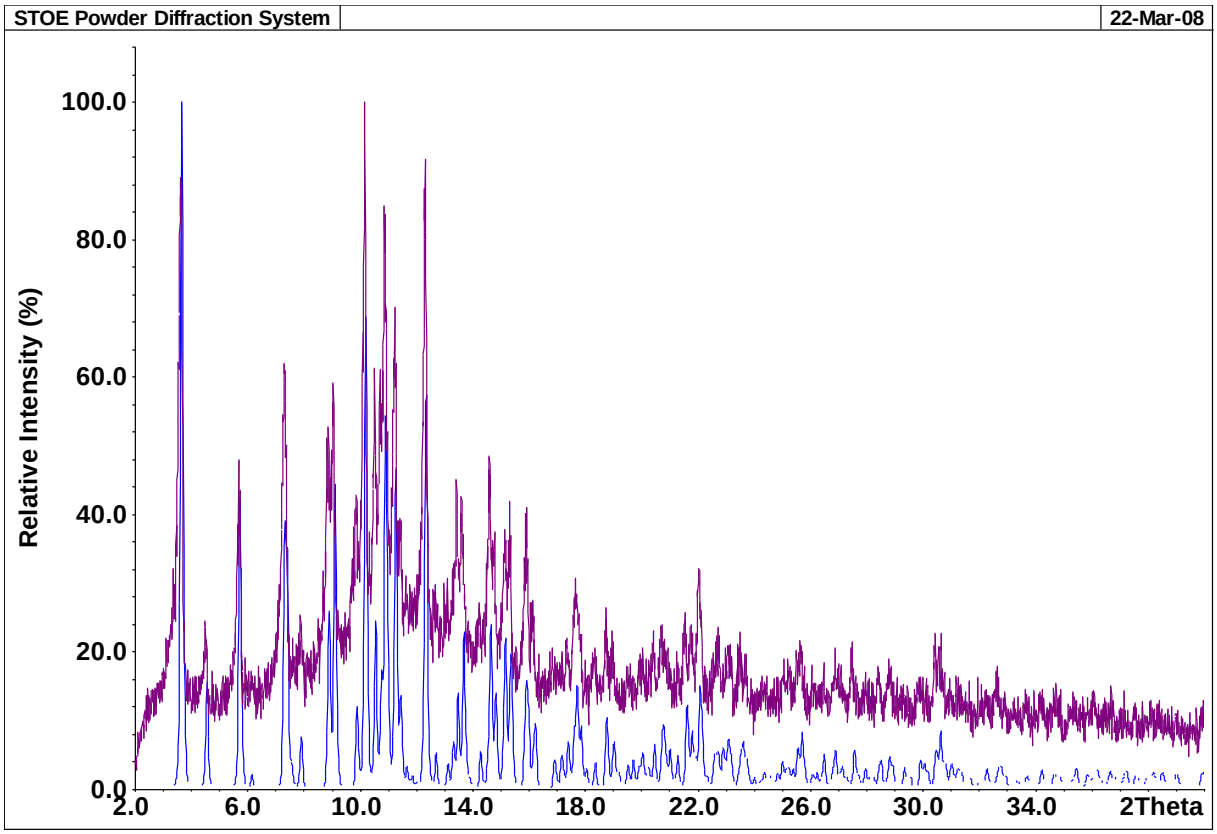

Fig. S22 X-ray powder diffractogram. Blue curve is simulated from single-crystal X-ray data of $^{3}_{\infty}$\{[Cd(μ_4-btre)(μ_2-btre)](ClO$_4$)$_2$\} (**9**). Purple curve is measured on a crystal sample of **9**.

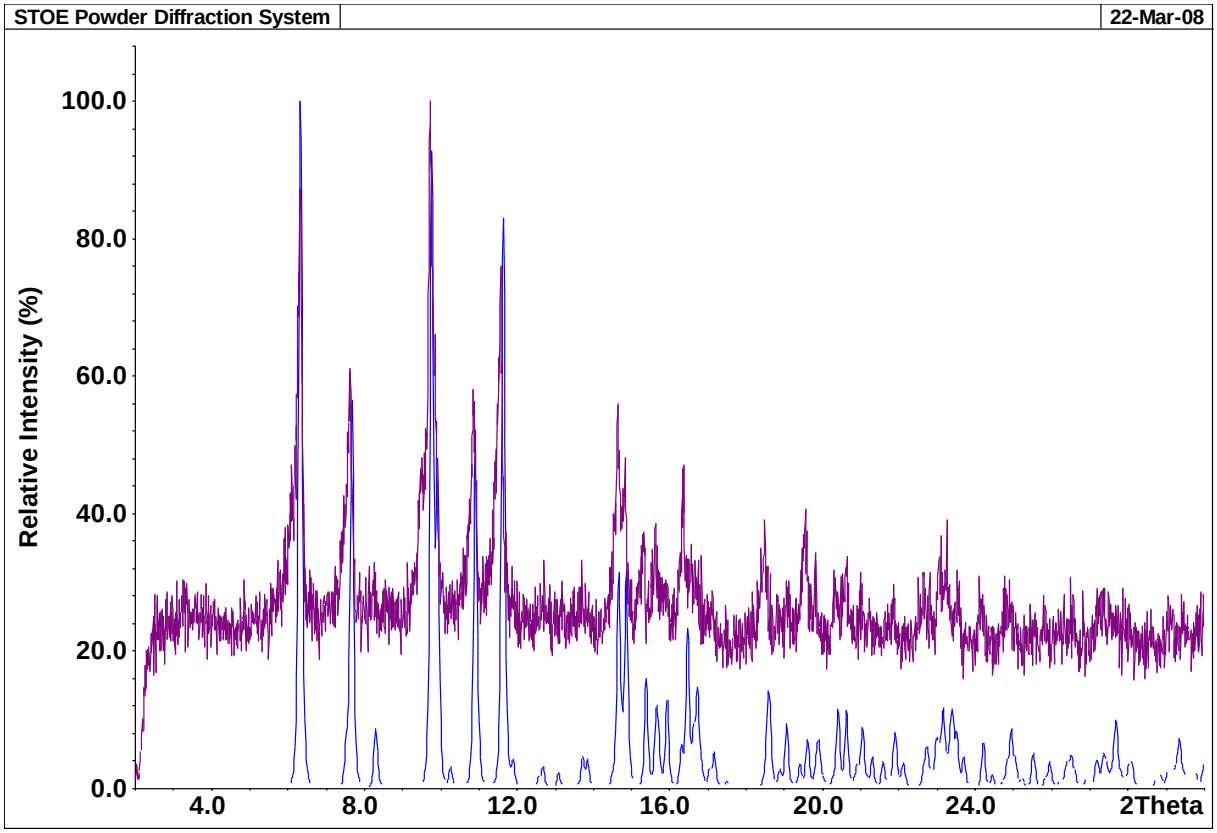

Fig. 23 X-ray powder diffractogram. Blue curve is simulated from single-crystal X-ray data of $^{3}_{\infty}$[Cu$_2$(μ_2-CN)$_2$(μ_4-btre)] (**10**). Purple curve is measured on a crystal sample of **10**.

Intermolecular interactions in 1-10

Table S1 C–H···N hydrogen bonding interactions in **1-3**, **8** and **9**.[a]

	D–H···A	D–H [Å]	H···A [Å]	D···A [Å]	D–H···A [°]	A···H···A' [°]	Sum [b]
1	C6–H6···N2^{6}	0.94	2.34	3.282(2)	175		
2	C6–H6···N2^{6}	0.98	2.35	3.291(5)	177		
3	C1–H1···N6$^{6'}$	0.94	2.38	3.248(5)	153		
	C5–H5···N2$^{7'}$	0.94	2.27	3.175(4)	161		
8	C1–H1···N5$^{4'''}$	0.94	2.46	3.336(6)	156		
	C1–H1···N5$^{6'''}$	0.94	2.46	3.336(6)	156'	32'	344
	C2–H2···N5$^{4'''}$	0.94	2.49	3.403(6)	163		
	C2–H2···N5$^{6'''}$	0.94	2.49	3.403(6)	163'	32'	358
9	C1–H1···N5$^{4'''}$	0.94	2.54	3.430(5)	157		
	C1–H1···N5$^{6'''}$	0.94	2.54	3.430(5)	157'	32'	346
	C2–H2···N5$^{4'''}$	0.94	2.55	3.465(4)	164		
	C2–H2···N5$^{6'''}$	0.94	2.55	3.465(4)	164'	32'	360

[a] D = Donor, A = acceptor. For found and refined atoms the standard deviations are given. Symmetry relations: 4'' = 0.5+x, 0.5–y, –0.5–z; 4''' = –0.5+x, 0.5–y, –0.5–z; 6 = 0.5–x, 0.5+y, 0.5–z; 6' = 0.5–x, 0.5+y, 1.5–z; 6'' = 0.5+x, y, –0.5–z; 6''' = –0.5+x, y, –0.5–z; 7' = 0.5–x, 0.5–y, 1–z.

[b] 3-center H-bond, bifurcated, sum of three angles (D–H···A + D–H···A' + A–H···A) about H should be 360°

Table S2 C–H···X (X = Cl, Br, O, S) hydrogen bonding interactions in **1-5**, **8** and **9**.[a]

D–H···A	D–H [Å]	H···A [Å]	D···A [Å]	D–H···A [°]
1 C4–H4A···Cl2^{6}	0.98	3.07	3.849(1)	137
2 C3–H3A···Br1$^{7'}$	0.98	2.92	3.856(3)	160
3 C6–H6···S^{5}	0.94	2.79	3.679(4)	159
4 C2–H2···Cl$^{2'''}$	0.94	2.81	3.577(5)	140
C3–H3A···Cl$^{2'v}$	0.98	2.85	3.620(5)	137
5 C2–H2···Br$^{2'''}$	0.94	2.90	2.682(2)	142
C3–H3A···Br$^{2'v}$	0.98	2.90	3.686(2)	138
8 C5–H4A···O2$^{3'}$	0.98	2.57	3.244(4)	126
C5–H4A···O2$^{5'}$	0.98	2.57	3.244(4)	126
C5–H5···O4$^{5'}$	0.94	2.44	3.096(7)	126
C6–H6···O1$^{6'}$	094	2.24	3.151(5)	163
C7–H7···O1$^{6'v}$	0.94	2.24	3.158(5)	164
C8–H8A···O2$^{6'v}$	0.98	2.34	3.245(5)	153
C8–H8B···O3$^{6'}$	0.98	2.44	3.149(5)	129
9 C5–H5···O4$^{5'}$	0.94	2.51	3.143(4)	125
C6–H6···O1$^{6'}$	094	2.33	3.246(3)	165
C7–H7···O1$^{6'v}$	0.94	2.32	3.222(3)	160
C8–H8A···O2$^{6'v}$	0.98	2.44	3.318(4)	149
C8–H8B···O3$^{6'}$	0.98	2.52	3.221(4)	128

[a] D = Donor, A = acceptor. For found and refined atoms the standard deviations are given. Symmetry relations: 2''' = –x, –y, 2–z; 2'^{v} = –x, 1–y, 2–z; 5 = –0.5+x, 0.5+y, z; 3 = 1–x, –0.5+y, –z; 5' = 1–x, 1–y, –z; 6 = 0.5–x, 0.5+y, 0.5–z; 6' = –0.5+x, y, 0.5–z; 6'^{v} = –1.5+x, y, 0.5–z; 7' = 0.5–x, 0.5–y, 1–z.

Table S3 Distances (d/Å) and angles (°) for the π-stacking interactions in **4-6** and **10**.[a]

compound ring(I)···ring(J)	d[Cg(I)···Cg(J)] [b]	α [c]	β [d]	γ [e]	d[Cg(I)···P(J)] [f]	d[Cg(J)···P(I)] [g]	d[a] [h]
4, triazolyl···triazolyl$^{2'''}$	3.489(3)	0.00	18.3	18.3	3.31	3.31	1.10
triazolyl···triazolyl$^{2'}$	4.214(3)	0.00	5.0	5.0	4.20	4.20	0.37
5, triazolyl···triazolyl$^{2'''}$	3.466(1)	0.02	18.1	18.1	3.29	3.29	1.08
triazolyl···triazolyl$^{2'}$	4.626(1)	0.02	9.2	9.2	4.57	4.57	0.74
6, N1-3···N1-3 $^{7''}$	3.986(4)	0.00	13.6	13.6	3.88	3.88	0.94
N4-6···N7-9 $^{1'}$	3.738(4)	6.95	26.0	23.0	3.44	3.36	--
10, triazolyl···triazolyl$^{3'''}$	3.505(2)	0.00	22.0	22.0	3.25	3.25	1.32
triazolyl···triazolyl$^{3''}$	5.100(2)	0.00	13.7	13.7	4.95	4.95	1.21

[a] For a graphical depiction of distances and angles in the assessment of the π-contacts, see Scheme S1. – [b] Centroid-centroid distance. – [c] Dihedral angle between the ring planes. – [d] Angle between the centroid vector Cg(I)···Cg(J) and the normal to the plane I ("slip angle"). – [e] Angle between the centroid vector Cg(I)···Cg(J) and the normal to the plane J. – [f] Perpendicular distance of Cg(I) on ring plane J. – [g] Perpendicular distance of Cg(J) on ring plane I. – [h] Slippage; distance between Cg(I) and perpendicular projection of Cg(J) on Ring I; parallel displacement between ring centroids from a perfect face-to-face alignment. Symmetry transformations: 1' = x, 1+y, z; 2' = 1–x, –y, 1–z; 2''' = –x, –y, 2–z; 3'' = –x, 1–y, –z; 3''' = 1–x, 1–y, 1–z; 7'' = 0.5–x, 1.5–y, –z.

Compounds not listed in Table S3 contain no or only π-stacking interactions which can be viewed as medium to weak in that they exhibit rather long centroid-centroid distances (Cg···Cg> 4.0 Å) together with large slip angles (β, γ > 30°) and vertical displacements (d > 2.0 Å). In comparison, strong π-stackings show rather short centroid-centroid contacts (< 3.8 Å), small slip angles (β, γ < 25°) and vertical displacements (d < 1.5 Å) which translate into a sizable overlap of the aromatic planes.

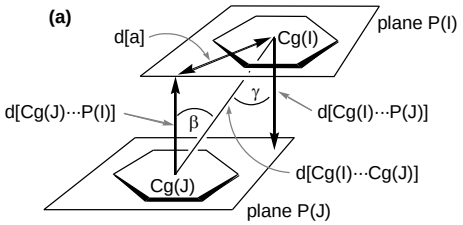

Scheme S1 Graphical presentation of the parameters used in Table S3 for the description of π-π stacking.

Tables of selected distances and angles in 1-10

Table S4 Selected bonds lengths (Å) and angles (°) in [{$ZnCl_2(\mu_2$-btre)$\}_2$], **1** and [{$ZnBr_2(\mu_2$-btre)$\}_2$], **2**.

	1 (X = Cl)	**2** (X = Br)
Zn–N1	2.015(12)	2.012(3)
Zn–N5^7	2.007(11)	2.005(3)
Zn–X1	2.241(4)	2.371(5)
Zn–X2	2.214(4)	2.352(5)
N5^7–Zn–N1	103.76(5)	104.26(11)
N5^7–Zn–X2	109.15(4)	108.65(8)
N1–Zn–X2	113.48(4)	113.04(8)
N5^7–Zn–X1	108.39(4)	110.45(8)
N1–Zn–X1	108.14(4)	107.77(8)
X1–Zn–X2	113.38(2)	112.36(2)

Symmetry relation in **1** and **2**: 7 = 0.5–x, 1.5–y, 1–z.

Table S5 Selected bonds lengths (Å) and angles (°) in $^1{}_\infty$[$Zn(NCS)_2(\mu_2$-btre)], **3**.

Zn–N1	2.005(3)	N8–Zn–N7	113.7(1)
Zn–N5^3	2.000(3)	N8–Zn–N5^3	108.1(1)
Zn–N7	1.922(3)	N8–Zn–N1	108.5(1)
Zn–N8	1.934(3)	N7–Zn–N1	108.5(1)
N7–C7	1.164(4)	N7–Zn–N5^3	116.1(1)
C7–S1	1.615(4)	N5^3–Zn–N1	101.0(1)
N8–C8	1.166(4)	Zn–N7–C7	170.6(3)
C8–S2	1.614(4)	Zn–N8–C8	167.7(3)

Symmetry relations: 3 = 0.5+x, 0.5+y, z.

Table S6 Selected bonds lengths (Å) and angles (°) in $^2{}_\infty$[$Cu_2(\mu_2$-Cl$)_2(\mu_4$-btre)], **4** and $^2{}_\infty$[$Cu_2(\mu_2$-Br$)_2(\mu_4$-btre)], **5**.

	4 (X = Cl)	**5** (X = Br)
Cu–N1	2.007(3)	2.009(2)
Cu–N2$^{2'}$	2.038(3)	2.024(2)
Cu–X$^{2''}$	2.343(1)	2.4616(4)
Cu–X	2.439(1)	2.5620(4)
Cu···Cu$^{2''}$	3.027(1)	3.176(4)
Cu$^{2'}$···Cu	3.616(7)	3.611(4)
N1–Cu–N2$^{2'}$	112.4(1)	112.25(7)
N1–Cu–X$^{2''}$	120.9(1)	114.62(5)
N2$^{2'}$–Cu–X$^{2''}$	105.6(1)	112.36(5)
N1–Cu–X	108.8(1)	111.32(6)
N2$^{2'}$–Cu–X	106.3(1)	103.61(6)
X–Cu–X$^{2''}$	101.48(4)	101.59(1)
Cu–X–Cu$^{2''}$	78.52(4)	78.41(1)

Symmetry relations in **4** and **5**: 1 = x, –1+y, z; 1' = x, –1+y, z; 1'' = –1+x, y, –1+z; 2 = –x, –y, 1–z; 2' = 1–x, –y, 1–z; 2'' = 1–x, 1–y, 2–z.

Table S7 Selected bonds lengths (Å) and angles (°) in $^2{}_\infty$\{[$Cd_6(\mu_3$-OH$)_2(\mu_3$-$SO_4)_4(\mu_4$-btre$)_3(H_2O)_6$](SO_4) · ~6H_2O\}, **6**.

Cd1–O21	2.273(5)	Cd2–O1	2.296(6)
Cd1–O4	2.278(4)	Cd2–N2	2.339(6)
Cd1–N5	2.308(5)	Cd2–N7	2.347(5)

Cd1–N1	2.318(6)	Cd3–O4	2.262(4)
Cd1–O13	2.341(5)	Cd3–O14	2.263(5)
Cd1–O22$^{4'}$	2.354(5)	Cd3–O3	2.285(5)
Cd2–O4	2.257(4)	Cd3–N8	2.299(6)
Cd2–O12	2.285(5)	Cd3–O2	2.333(5)
Cd2–O23^{1}	2.292(5)	Cd3–N4	2.355(6)

O21–Cd1–O4	162.2(2)	O12–Cd2–N2	93.4(2)
O21–Cd1–N5	93.8(2)	O23^{1}–Cd2–N2	96.1(2)
O4–Cd1–N5	95.3(2)	O1–Cd2–N2	92.1(3)
O21–Cd1–N1	85.8(2)	O4–Cd2–N7	86.8(2)
O4–Cd1–N1	86.9(2)	O12–Cd2–N7	93.4(2)
N5–Cd1–N1	173.0(2)	O23^{1}–Cd2–N7	82.0(2)
O21–Cd1–O13	105.7(2)	O1–Cd2–N7	97.8(3)
O4–Cd1–O13	90.4(2)	N2–Cd2–N7	169.1(2)
N5–Cd1–O13	85.3(2)	O4–Cd3–O14	88.1(2)
N1–Cd1–O13	88.1(2)	O4–Cd3–O3	177.3(2)
O21–Cd1–O22$^{4'}$	78.2(2)	O14–Cd3–O3	90.7(2)
O4–Cd1–O22$^{4'}$	86.1(2)	O4–Cd3–N8	89.6(2)
N5–Cd1–O22$^{4'}$	92.7(2)	O14–Cd3–N8	92.6(2)
N1–Cd1–O22$^{4'}$	94.1(2)	O3–Cd3–N8	88.0(2)
O13–Cd1–O22$^{4'}$	175.8(2)	O4–Cd3–O2	89.5(2)
O4–Cd2–O12	85.7(2)	O14–Cd3–O2	170.3(2)
O4–Cd2–O23^{1}	122.8(2)	O3–Cd3–O2	92.1(2)
O12–Cd2–O23^{1}	150.5(2)	N8–Cd3–O2	96.8(2)
O4–Cd2–O1	161.0(2)	O4–Cd3–N4	92.6(2)
O12–Cd2–O1	75.7(2)	O14–Cd3–N4	85.6(2)
O23^{1}–Cd2–O1	76.1(2)	O3–Cd3–N4	89.7(2)
O4–Cd2–N2	85.3(2)	N8–Cd3–N4	177.0(2)
		O2–Cd3–N4	85.1(2)

Symmetry relations in **6**: 1 = x, –1+y, z; 4' = 0.5–x, –0.5+y, 0.5–z.

Table S8 Selected bonds lengths (Å) and angles (°) in $^{3}_{\infty}$\{[Cu(μ_4-btre)]$ClO_4 \cdot$ ~0.25H_2O\}, **7**.

Cu–N1	1.996(14)	Cu–N2^{5}	2.075(16)

N1–Cu–N1^{2}	117.52(8)	N1–Cu–N2^{6}	111.57(6)
N1–Cu–N2^{5}	109.48(6)	N2^{5}–Cu–N2^{6}	94.95(10)

Symmetry relations: 2 = –x, y, 0.5–z; 5 = –x, –y, –z; 6 = x, –y, 0.5+z.

Table S9 Selected bond lengths (Å) and angles (°) in $^{3}_{\infty}$\{[Zn(μ_4-btre)(μ_2-btre)]$(ClO_4)_2$\}, **8** and $^{3}_{\infty}$\{[Cd(μ_4-btre)(μ_2-btre)]$(ClO_4)_2$\}, **9**.

	8		**9**
Zn–N1	2.160(4)	Cd–N1	2.344(3)
Zn–N2^{4}	2.159(4)	Cd–N2^{4}	2.353(3)
Zn–N6	2.175(3)	Cd–N6	2.327(2)
Zn–N7^{4}	2.210(3)	Cd–N7^{4}	2.349(2)

N1–Zn–N7^{4}	91.2(1)	N1–Cd–N7^{4}	89.97(7)
N2^{4}–Zn–N1	179.8(2)	N2^{4}–Cd–N1	178.23(11)
N2^{4}–Zn–N6	92.00(1)	N2^{4}–Cd–N6	89.96(8)
N2^{4}–Zn–N7^{4}	88.9(1)	N2^{4}–Cd– N7^{4}	91.30(7)
N6–Zn–N1	87.9(2)	N6–Cd–N1	88.77(7)
N6–Zn–N6^{7}	87.3(2)	N6–Cd–N6^{7}	88.50(1)
N6–Zn–N7^{6}	93.2(1)	N6–Cd–N7^{6}	91.79(7)
N6–Zn–N7^{4}	179.0(1)	N6–Cd–N7^{4}	178.71(8)
N7^{4}–Zn–N7^{6}	86.4(2)	N7^{4}–Cd–N7^{6}	87.89(10)

Symmetry relations in **8** and **9**: 4 = 0.5+x, 0.5–y, 0.5–z; 6 = 0.5+x, y, 0.5–z; 7 = x, 0.5–y, z.

Table S10 Selected bonds lengths (Å) and angles (°) in $^{3}_{\infty}[Cu_2(\mu_2\text{-}CN)_2(\mu_4\text{-}btre)]$, **10**.

Cu–C4	1.906(3)	N4–Cu–N1	100.96(10)
Cu–N4^{4}	1.998(3)	C4–Cu–N2^{3}	110.30(11)
Cu–N2^{3}	2.080(2)	N4–Cu–N2^{3}	106.39(10)
Cu–N1	2.084(2)	C4–Cu–N4	119.55(11)
C4–N4	1.145(4)		
		N4–C4–Cu	173.6(3)
N2^{3}–Cu–N1	103.03(9)	C4–N4–Cu^{3}	165.7(2)
C4–Cu–N1	114.95(11)		

Symmetry relations: 1 = 1+x, y, –1+z; 3 = –x, 1–y, 1–z; 3' = 1–x, 1–y, –z; 4 = –0.5+x, 1.5–y, –0.5+z; 4' = 0.5+x, 1.5–y, 0.5+z.

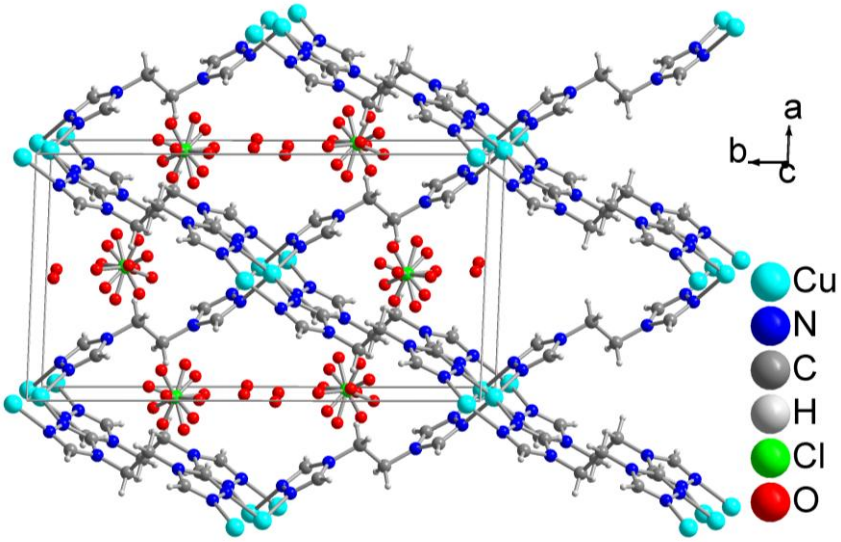

Fig. S24 3D framework in $^{3}_{\infty}\{[Cu(\mu_4\text{-}btre)]ClO_4 \cdot \sim 0.25H_2O\}$ **7** with disordered perchlorate ions and crystal water in channels.

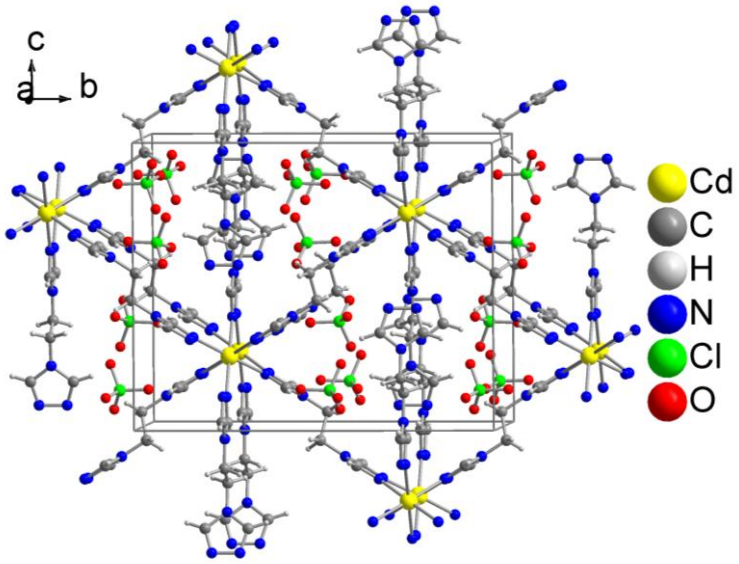

Fig. S25 3D framework in $^{3}_{\infty}\{[Zn(\mu_4\text{-}btre)(\mu_2\text{-}btre)](ClO_4)_2\}$ **8** and $^{3}_{\infty}\{[Cd(\mu_4\text{-}btre)(\mu_2\text{-}btre)](ClO_4)_2\}$ **9** with perchlorate ions in the trigonal channels.

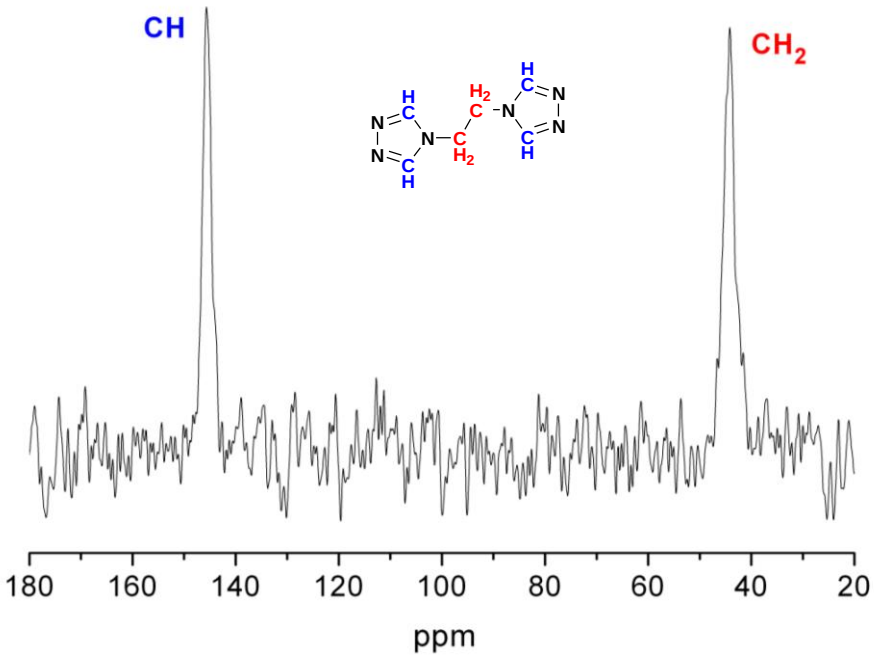

Fig. S26 ^{13}C CPMAS NMR spectrum for 1,2-bis(1,2,4-triazol-4-yl)ethane and schematic drawing of the ligand molecule. Peak positions: 145.6 and 44.1 ppm.

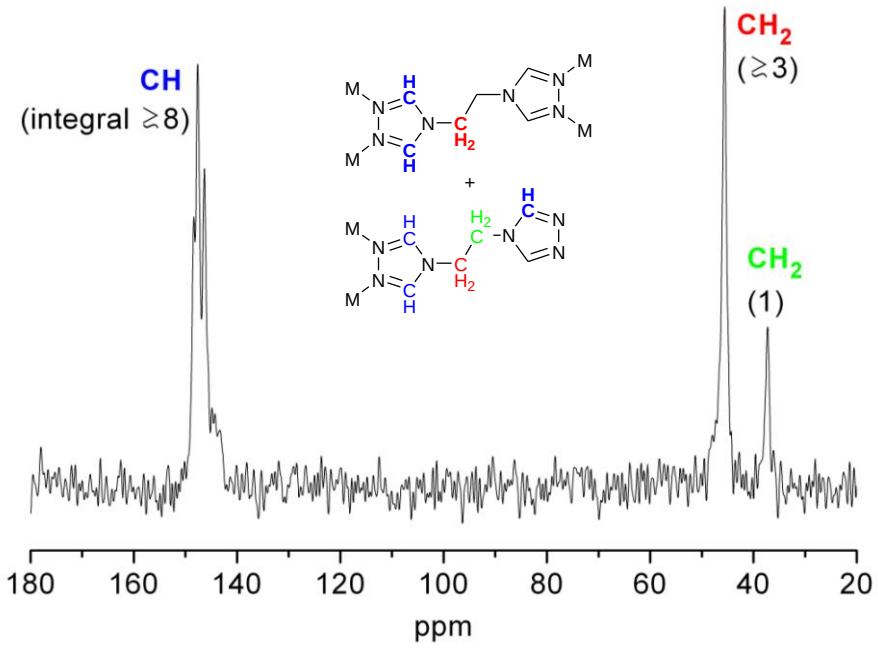

Fig. S27 ^{13}C CPMAS NMR spectrum for **9** and schematic drawing of the building unit with the unique C atoms as atom symbols. All atoms of the μ$_2$-κ*N*1:*N*2-bridging, dangling btre ligand have half-occupancy (indicated by plain font style). Integral of CH_2 resonance below 40 set to 1. Peak positions: 148.4, 147.6, 146.3, 144.3, 45.6 and 37.2 ppm.

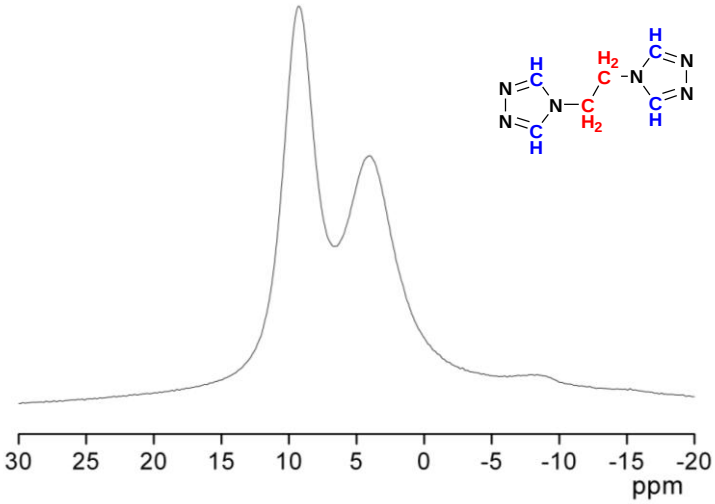

Fig. S28 ^{1}H MAS NMR spectrum for 1,2-bis(1,2,4-triazol-4-yl)ethane and schematic drawing of the ligand molecule.

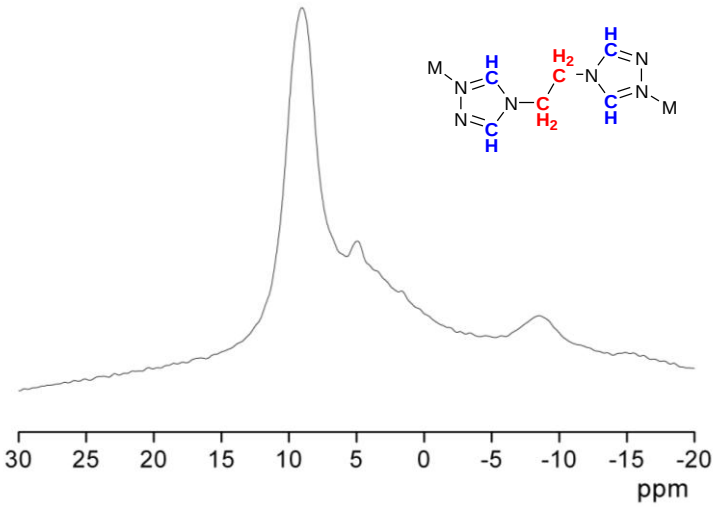

Fig. S29 ^{1}H MAS NMR spectrum for **1** and schematic drawing of the building unit with the unique H atoms given as atom symbols.

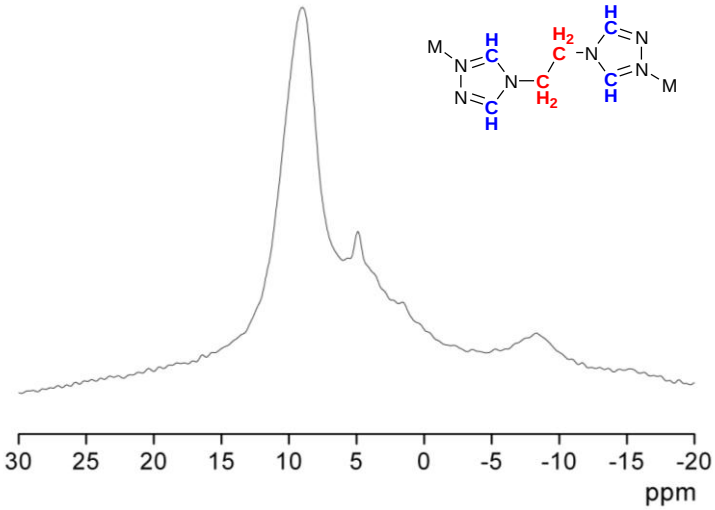

Fig. S30 ^{1}H MAS NMR spectrum for **2** and schematic drawing of the building unit with the unique H atoms given as atom symbols.

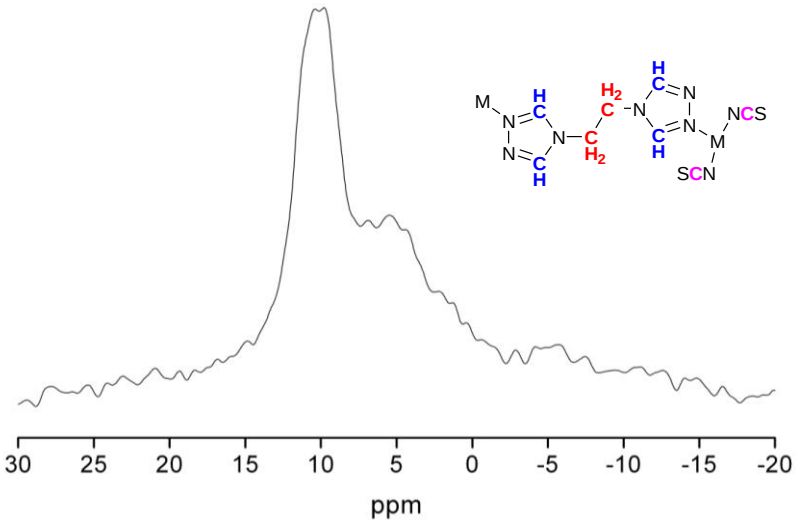

Fig. S31 ^{1}H MAS NMR spectrum for **3** and schematic drawing of the building unit with the unique H atoms given as atom symbols.

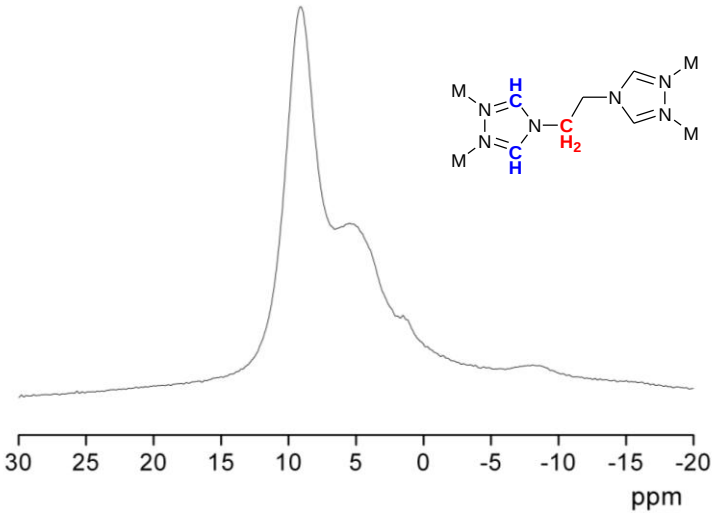

Fig. S32 ^{1}H MAS NMR spectrum for **4** and schematic drawing of the building unit with the unique H atoms given as atom symbols.

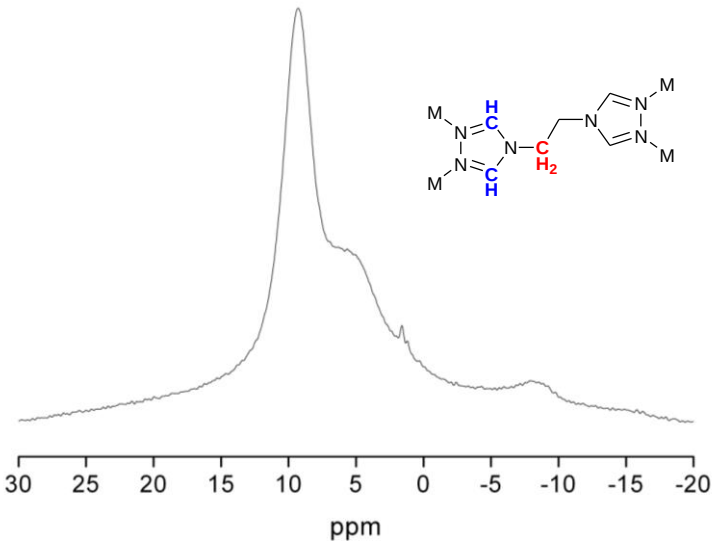

Fig. S33 ^{1}H MAS NMR spectrum for **5** and schematic drawing of the building unit with the unique H atoms given as atom symbols.

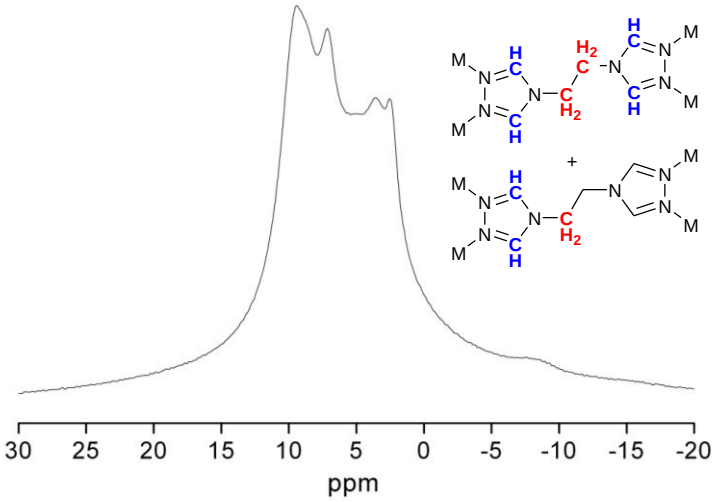

Fig. S34 ^{1}H MAS NMR spectrum for **6** and schematic drawing of the building unit with the unique H atoms given as atom symbols.

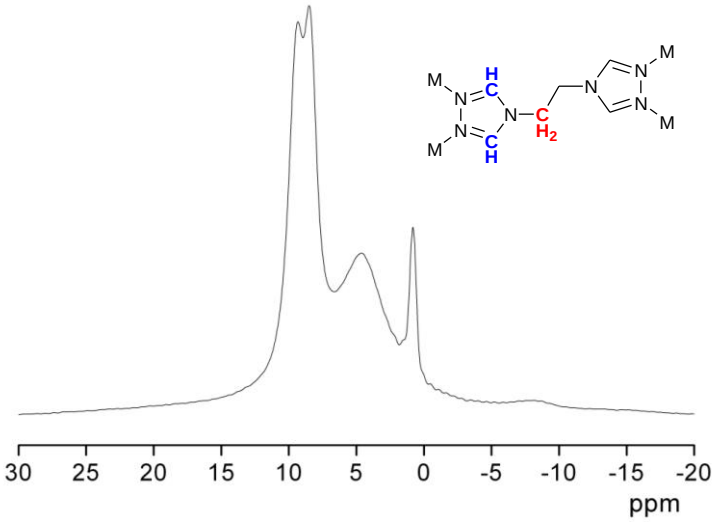

Fig. S35 ^{1}H MAS NMR spectrum for **7** and schematic drawing of the building unit with the unique H atoms given as atom symbols.

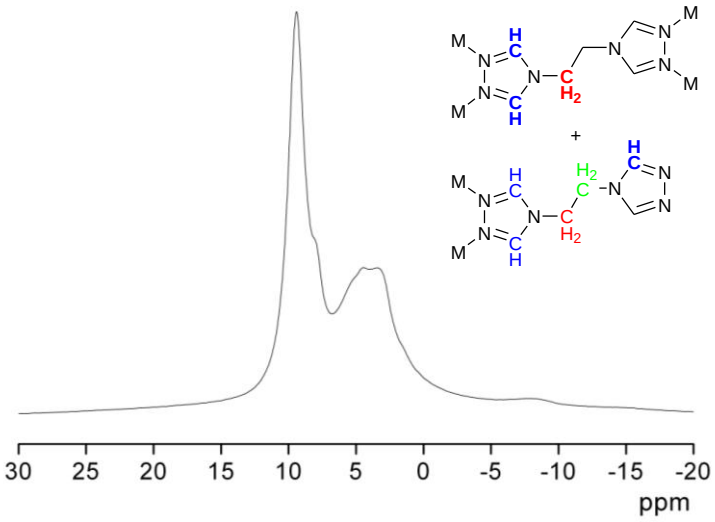

Fig. S36 ^{1}H MAS NMR spectrum for **8** and schematic drawing of the building unit with the unique H atoms given as atom symbols.

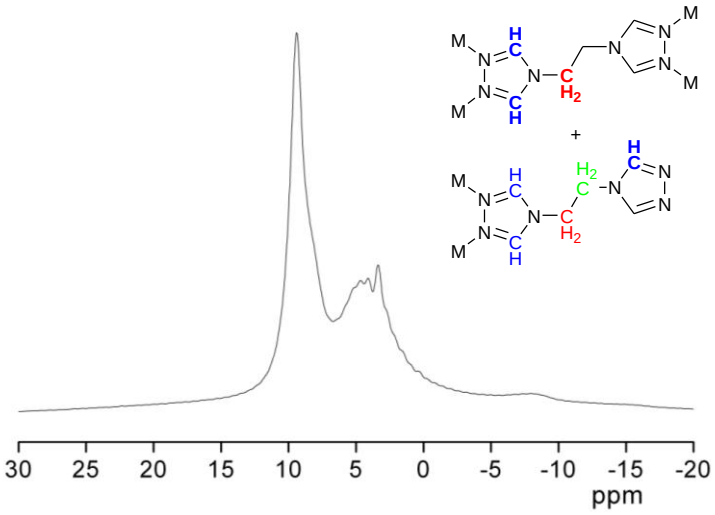

Fig. S37 ^{1}H MAS NMR spectrum for **9** and schematic drawing of the building unit with the unique H atoms given as atom symbols.

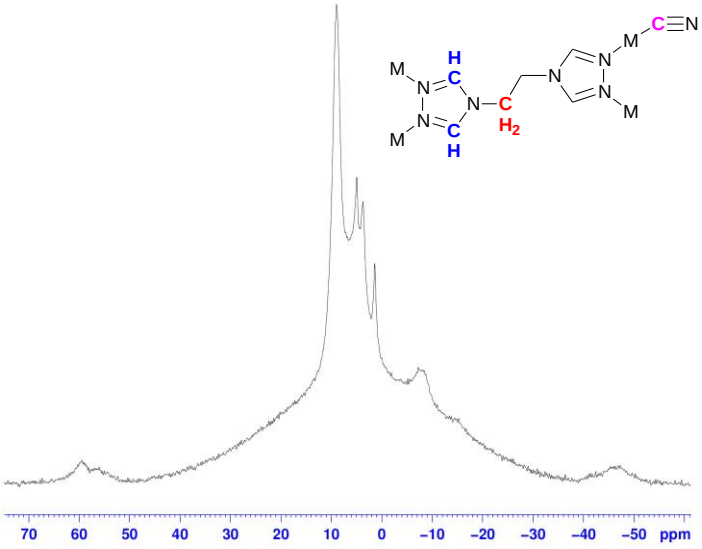

Fig. S38 ^{1}H MAS NMR spectrum for **10** and schematic drawing of the building unit with the unique H atoms given as atom symbols.